Frequency Domain Model-Based Intracranial Pressure Estimation

by

Irena T. Hwang

Submitted to the Department of Electrical Engineering and Computer Science
in partial fulfillment of the requirements for the degree of

Master of Engineering in Electrical Engineering

at the

MASSACHUSETTS INSTITUTE OF TECHNOLOGY

May 2012

Author .....
Department of Electrical Engineering and Computer Science
May 24, 2012

Certified by.....
George C. Verghese
Professor of Electrical Engineering
Thesis Supervisor

Certified by.....
Faisal M. Kashif
Senior Engineer, Masimo Corp. Research and Development
Technology Boards
Thesis Supervisor

Accepted by .....
Dennis M. Freeman
Chairman, Department Committee on M.Eng. Students

Frequency Domain Model-Based Intracranial Pressure Estimation

by

Irena T. Hwang

Submitted to the Department of Electrical Engineering and Computer Science
on May 24, 2012, in partial fulfillment of the
requirements for the degree of
Master of Engineering in Electrical Engineering

Abstract

Elevation of intracranial pressure (ICP), the pressure of the fluid surrounding the brain, can require urgent medical attention. Current methods for determining ICP are invasive, require neurosurgical expertise, and can lead to infection. ICP measurement is therefore limited to the sickest patients, though many others could potentially benefit from availability of this vital sign. We present a frequency-domain approach to ICP estimation using a simple lumped, linear time-invariant model of cerebrovascular dynamics. Preliminary results from 28 records of patients with severe traumatic brain injury are presented and discussed. Suggestions for future work to improve the estimation algorithm are proposed.

Thesis Supervisor: George C. Verghese
Title: Professor of Electrical Engineering

Thesis Supervisor: Faisal M. Kashif
Title: Senior Engineer, Masimo Corp. Research and Development Technology Boards

Acknowledgments

I would like to acknowledge the people who were instrumental in supporting, motivating, and guiding me along this academic and personal journey.

First and foremost, I wish to thank Dr. Faisal Kashif for all of his patience, wisdom, and time. Faisal is the kind of mentor every student dreams of: always understanding, willing to meet at a moment's notice, and invariably optimistic and encouraging. Through countless hours of discussion and over even more cups of hot beverages, Faisal taught me to appreciate the beauty of research, and to persevere when faced with the frustrations of investigation.

Many thanks are also due to the Computational Physiology and Clinical Inference (CPCI) group. Insightful, and sometimes amusing, group meetings provided much-needed feedback and inspiration. Professor George Verghese and Dr. Thomas Heldt, especially, were keen sources of ideas for project direction and guidance.

To my family and friends, so much thanks for your support. My parents and sister supplied constant encouragement, and I could not have completed this project without our late-night phone calls and their cheering-on. Ankit Gordhandas, a driving force in my joining CPCI in the first place, provided endless hours of lighthearted jokes and serious discussion.

And last, but certainly not least, Kevin Fischer has been an unwavering pillar of support and patience (so much patience). I sure as heck could not have done this without him by my side.

Contents

List of Figures

Chapter 1

Introduction

As the most complex organ in the human body and center of all nervous functions, the brain is extremely sensitive to changes in blood flow. Too little blood can deprive cerebral tissue of oxygen, ultimately resulting in tissue death, while too much blood can result in compression and damage of brain tissue [1]. Cerebral blood flow is tightly regulated over significant variation in arterial blood pressure, via a process called cerebral autoregulation in which cerebral arteries change their diameters in response changes in blood flow.

The pressure of the cerebrospinal fluid surrounding the brain, or intracranial pressure (ICP), plays a large role in determining the flow of blood perfusing cerebral tissue. Cerebral perfusion pressure (CPP) is the difference between mean arterial pressure (MAP) and ICP: CPP = MAP − ICP. ICP is typically maintained by the human body at 7-15 mmHg when the person is supine. Elevated ICP, or intracranial hypertension, is defined as ICP levels greater than 15 mmHg. Urgent intervention in cases of traumatic brain injury is required if ICP exceeds 20-25 mmHg. However, ICP can rise dramatically as a result of brain injury, hydrocephalus, tumor and stroke. Elevated ICP can cause damage to brain tissue by reducing CPP and thus depriving the tissue of desired blood supply, and in some cases even result in rapid death. As a result, it is of utmost importance to monitor ICP in patients with neurological conditions, especially brain injury, and to provide immediate intervention if ICP is elevated.

In this chapter we review current methods for monitoring ICP and provide an overview of noninvasive approaches to ICP estimation, including a recent approach [2] that forms the basis for explorations in this thesis.

1.1 Review of ICP Monitoring Methods

1.1.1 Invasive Monitoring Methods

Currently, clinical methods for monitoring ICP are limited to invasive surgical procedures that require placement of intracranial transducers via burr holes drilled into the skull. Fig. 1-1 shows several possible placements of the transducers. We briefly describe each of the shown monitoring approaches below.

The most reliable monitoring method requires placement of a fluid-filled catheter inside the lateral ventricle; the catheter is then connected to an external strain-gauge. The intraventricular catheter method has been in use since the 1950's, and is considered the "gold-standard" ICP measurement [3]. This approach additionally allows for sampling and drainage of excess cerebrospinal fluid (CSF). However, placement of the ventricular probe requires a high degree of surgical precision, and this method can be compromised by catheter clogging or ventricle compression. Furthermore, as it is the most invasive method, there exists a greater risk of infection or hemorrhage [4].

Another method of ICP monitoring is placement of a pressure-sensor probe in the brain parenchyma. This approach is very common, though it is slightly less accurate than the intraventricular catheter. While the parynchemal probe can be placed more easily than the ventricular probe, the method still carries significantly high risk of infection and bleeding, and does not allow for draining of CSF [5].

Other monitoring methods access CSF in the space between the arachnoid membrane and the brain. These methods bypass passage of transducers through brain tissue, but still require penetration of the skull. They are less accurate and do not allow drainage of CSF, but are still used due to the lesser degree of invasiveness. For

subdural measurements, a subdural screw or bolt is inserted into a hole in the skull, and a transducer electrode is placed through the dura mater. However, the subdural bolt has a tendency to become blocked, and provides a lower reading of ICP due to the pressure drop associated with CSF flow from the ventricles to the subdural space [6]. Placement of an epidural sensor between the skull and dural tissue is least invasive, but is also the least accurate of the methods currently in use.

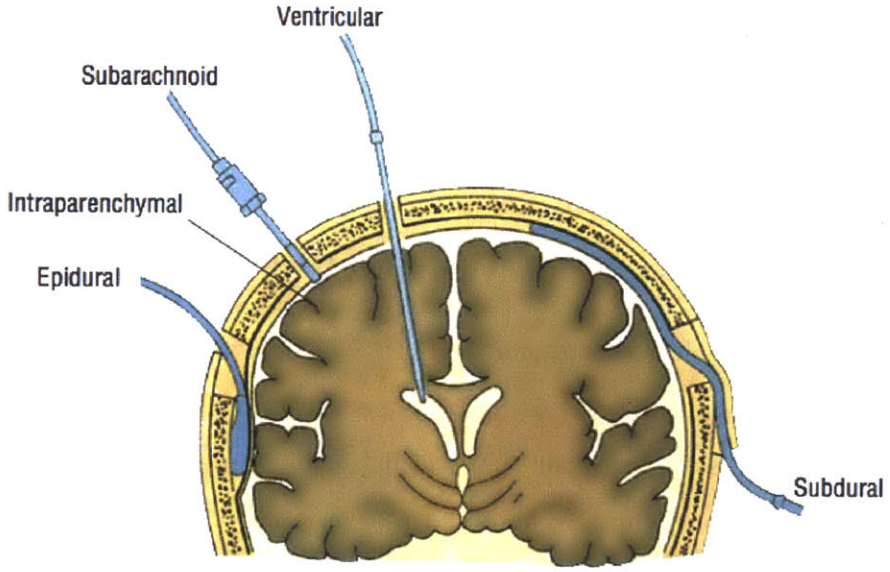

Figure 1-1: Figure showing placement of intracranial pressure transducers, adapted from [7].

Finally, an alternative method is the lumbar puncture or spinal tap, which accesses CSF via the spinal canal. A needle connected to a pressure transducer is inserted into the spinal canal below the first lumbar vertebra. Typically used in cases where ICP is believed to be not highly elevated, lumbar punctures provide an intermittent measure of ICP. However, during intracranial hypertension this method is extremely risky, as a large pressure gradient can build between the the brain and point of puncture, inducing herniation of the brain through the spinal column and sudden death [8]. Furthermore, ICP can differ significantly from the pressure in the spinal canal, rendering lumbar puncture unsuitable for continuous, accurate monitoring of ICP.

Despite minor differences in invasiveness, accuracy and utility for relieving in-

tracranial hypertension, each of the monitoring methods described above is an extremely invasive procedure and carries high risk of infection, bleeding and pain. As a result, ICP is monitored in only the sickest patients, such as patients with a Glasgow Coma Scale score of 3-8 as per the Brain Trauma Foundation guidelines [9]. However, a continuous and noninvasive form of ICP monitoring could be very beneficial to patients with varying degrees of brain injury, and other relatively mild neurological conditions. This at-risk population includes athletes, construction workers and soldiers in combat, for example. Regular, noninvasive ICP monitoring could allow for early detection of intracranial hypertension, thus guiding diagnosis and therapy to prevent further brain injury.

1.1.2 Approaches to Noninvasive ICP Estimation

There have been many efforts to estimate ICP noninvasively. However, despite the large volume of investigation, no method has yet been adopted for routine clinical use. Noninvasive ICP estimation methods still lag far behind conventional invasive methods in terms of accuracy, application to large patient populations, and utility in continuous monitoring situations. Furthermore, most of the proposed approaches require training and/or calibration data, are not patient-specific, and are not suited for continuous clinical monitoring. However, a recent model-based estimation method has shown promising results that are comparable to the current "gold-standard" intraventricular probe. We describe a few main areas of noninvasive ICP estimation research, and conclude by describing the model-based approach.

Some studies focus on inferring ICP from nearby physiological pressures. The eye, for example, has been used as a window into the otherwise difficult-to-penetrate cranium. While it has been shown that intraocular pressure, or the fluid pressure inside the eye, does not correlate with ICP, other studies have demonstrated a relationship between arterial flow and ICP in the intracranial segment of the optical artery. These studies are based on a "balance of pressure" idea, and apply pressure on the optical artery via pressure on the eyeball until flow in the extra-cranial segment of the artery matches that of the intracranial segment [10]. Although the method

reported extremely low error means over a set of 57 patients, it requires a complex setup that includes application of a rigid chamber over the eye, an external pressure source, and focusing of a two-depth Doppler ultrasound, which particularly requires technical expertise. Thus, this method is also ill-suited for continuous ICP monitoring, since application of pressure to the eye is not only equipment-heavy, but also causes discomfort to the patient.

In addition to physiologically-based noninvasive ICP estimation methods, there also exist several purely computational approaches that extract relationships between measured data and ICP. For example, Hu et al. [11] propose a data-mining technique that employs a support-vector-machine to relate blood pressure and flow waveforms to ICP. Other machine-learning techniques also utilize huge sets of patient records as training data in order to increase accuracy. However, these methods have poor estimation performance when applied to a general population, and further require large volumes of invasively obtained training data which may not have any similarities with a particular case of interest.

While most noninvasive approaches attempt to either isolate a physiological phenomenon or rely completely on numerical methods in order to estimate ICP, physiological models of the cerebrovascular system are also of significant interest. Various models of the complete cerebrovascular system have been proposed, detailing the relationship between fluid pressure, flow, and physiological compartments of the brain. One such complete model proposed by Sorek et al. is shown in Fig. 1-2, and represents mechanical properties of the cerebrovascular system in terms of seven compartments: brain tissue, arteries, capillaries, veins, venous sinus, jugular bulb, and CSF [12]. The compartments are represented by resistance and compliance elements.

While the model by Sorek et al. summarizes the mechanical properties of the cerebrovascular system, it does not address the issue of time-dependent dynamics. Considerations such as modeling venous collapse with a Starling resistor, autoregulation of cerebrovasculature, and CSF dynamics related to cerebral blood circulation are missing from this model, but are addressed in the model presented by Ursino and Lodi in [13]. Fig. 1-3 shows their electrical circuit analog model of the cerebrovas-

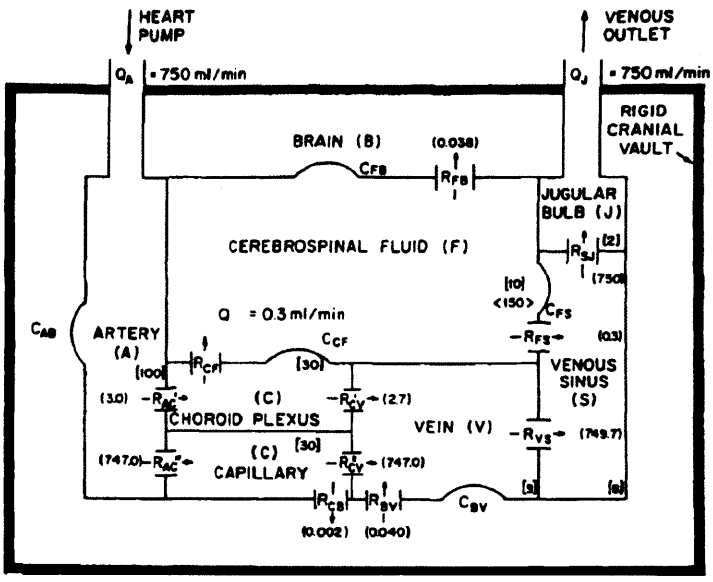

Figure 1-2: Lumped-parameter model of the cerebrovascular system proposed by Sorek et al. [12]. Nominal values of pressure and flow are specified in braces and parentheses, respectively.

cular system. Note that the model distinguishes arteries from arterioles and large and small veins. In addition, the model contains nonlinear elements that capture the dynamics of the cerebrovascular system.

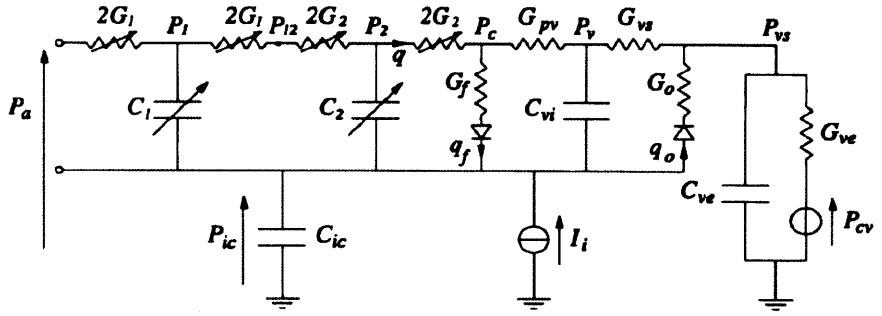

Figure 1-3: Electric circuit model of cerebrovascular system proposed by Ursino and Lodi [13]. Note the nonlinear circuit elements.

Although most models, including the two above, were created in order to simply distill the cerebrovascular system into a lumped representation, they can serve as a good platform for identifying physiological parameters, including vascular compliance, resistance, and even ICP. However, these models are too complex for any kind of

parameter estimation, and their use remains limited to simulations and academic demonstrations.

In [14], Kashif et al. present a simplified model of the cerebrovascular system. They also present an ICP estimation algorithm that uses widely available physiological waveforms. Their model lumps the entire cerebrovasculature into only resistance and compliance circuit components. Kashif et al. report validation over 45 patient records with error statistics comparable to some invasive ICP monitoring methods in current clinical use. Because their method is model-based and uses waveforms readily available in the clinic, it is a very promising option uniquely equipped to meet the demands of continuous, noninvasive ICP estimation. In the following section, we discuss the benefits of the Kashif et al. algorithm, and motivate the formulation of a frequency-domain model-based algorithm.

1.2 Motivation

The noninvasive ICP estimation method proposed in [14] is unique in several ways. First, the method is model-based and requires no training data or calibration prior to use. Second, while the method relies mainly on computation and waveform analysis in order to estimate ICP, it is rooted in a mechanistic view of the system that is easily understood by both clinicians and engineers alike. The method utilizes waveforms that are readily available in the clinic and whose acquisition is both facile for clinicians and pain-free for the patient. Finally, it is suitable for continuous monitoring and does not require neurosurgical expertise or equipment.

In [2], the authors demonstrated very promising results from preliminary estimation compared with invasive measurements obtained via parenchymal probe. However, investigation into the method revealed that signal quality and waveform noise has a profound effect on the quality of generated ICP estimates. This prompted investigation of alternative parameter estimation approaches that are relatively immune to measurement noise and artifact. The observation that most input data noise is high frequency in origin inspired an effort to examine the estimation algorithm in the fre-

quency domain. It is hoped that a frequency domain-based alternative algorithm will be potentially robust against specific data artifacts that are less tolerable to the time domain-based algorithm. This method may be used in combination with the time domain algorithm. Furthermore, the frequency domain-based algorithm corroborates the pervious results, and adds confidence to the simple model in [14].

1.3 Thesis Objectives and Organization

1.3.1 Thesis Objectives

This thesis presents a frequency domain (FD) ICP estimation algorithm based on the time domain (TD) algorithm presented in [14]. The FD estimation algorithm draws from the qualities of the TD algorithm mentioned above, and also benefits from characteristics that are unique to the frequency domain. We address three main objectives in this thesis.

- We develop the ICP estimation algorithm in the frequency domain.
- We compare the performance of FD estimation against invasive measurements over a population of 28 patient records, and validate the simplified model of the cerebrovascular system.
- We discuss characteristics of records that are intractable to estimation in the frequency domain, and present our findings for preemptive identification of cases that require alternate estimation approaches.

1.3.2 Thesis Organization

The thesis is organized as follows. The next chapter presents the physiology underlying the simplified cerebrovascular model from [14]. The simplified model and TD ICP estimation algorithm are reviewed in detail, and a brief overview is given to familiarize the reader with the algorithm steps. We also describe the input measurements used for estimation, and provide a brief description of their acquisition.

In Chapter 3, we introduce the FD estimation algorithm. We review the equations underlying parameter estimation, and the method used to solve for the parameters. We also review the pre-processing steps necessary prior to ICP estimation. In this chapter, we detail FD-specific investigations and their effect on the algorithm. Finally, we give a summary of the FD algorithm and clearly define all algorithm parameters used for estimation.

Chapter 4 presents the results of FD estimation for 28 patient records. We discuss in detail the results and characterize algorithm performance. We compare the results to both invasive ICP measurements as well as noninvasive TD estimates. Additionally, we discuss salient characteristics of records intractable to FD estimation. We propose tentative conditions for identifying records that possess the same characteristics, and recommend the best alternative for obtaining ICP information.

We conclude the thesis with Chapter 5, and make suggestions for future work.

Chapter 2

Cerebrovascular Physiology and Simplified Model for ICP Estimation

In this chapter, we review the relevant anatomy and physiology of the cerebrovascular system. We briefly describe consequences of elevated ICP, and the pathophysiology of brain injury. We then examine the simplified model presented in [14], and give an overview of TD estimation of ICP. Understanding of the cerebrovascular physiology and simplified model prepares us for development of the FD estimation algorithm in the next chapter.

2.1 Cerebrovascular Physiology

Blood and nutrients are supplied to the brain via a cerebrovascular network, which also removes CO_2 and other metabolic waste products. Cerebral blood flow (CBF) is normally around 50 mL of blood per 100 g of brain tissue per minute, and is tightly regulated in order to meet the brain's metabolic demands. Hyperemia, or too much blood, can result in compression and damage of brain tissue. Ischemia, or too little blood, occurs if the blood flow is less than 8 mL per 100 g per minute, and results in tissue death. Blood is circulated within the brain via a vascular network of cerebral

arteries and veins, described below.

Cerebro-arterial system

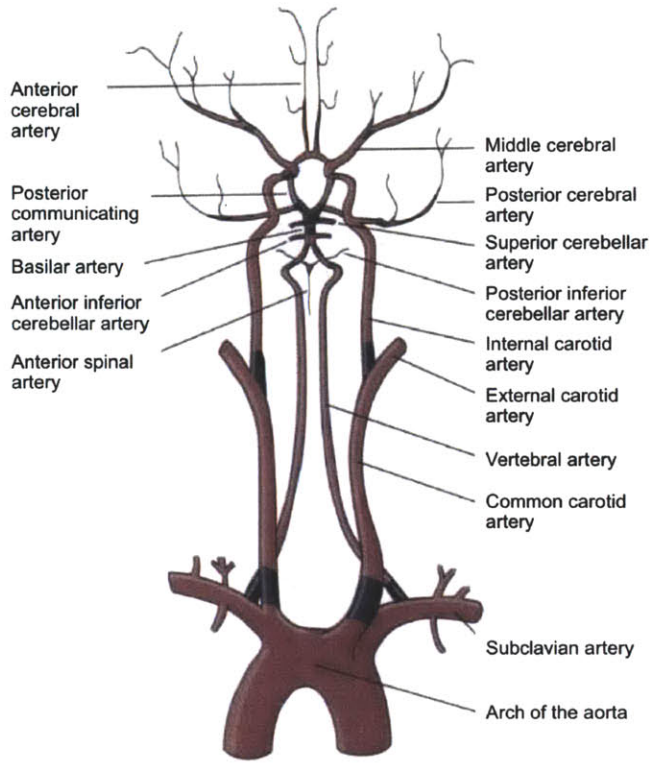

Figure 2-1: Cerebral blood circulation: arteries [8].

Blood flow arrives at the brain via two major sets of vessels: the left and right common carotid arteries and the left and right vertebral arteries. Fig. 2-1 shows the orientation of the arteries. The common carotid arteries split into the external and internal carotids, which supply blood to the scalp and face and the anterior part of the cerebrum, respectively. Blood flow through the internal carotid arteries is extremely vital: loss of blood flow to the frontal lobes could result in weakness or paralysis on the opposite side of the body. Blockages in either of the vertebral arteries are equally impairing.

The carotid and vertebral arteries join at the base of the brain, forming what is known as the Circle of Willis. In each of the two (left and right) hemispheres, three main arteries, the anterior cerebral, posterior cerebral and the middle cerebral, branch

from the Circle and supply blood to the bulk of the brain. The middle cerebral artery (MCA) in the left and right hemisphere supplies blood to the majority of brain tissue on each side.

Cerebro-venous system

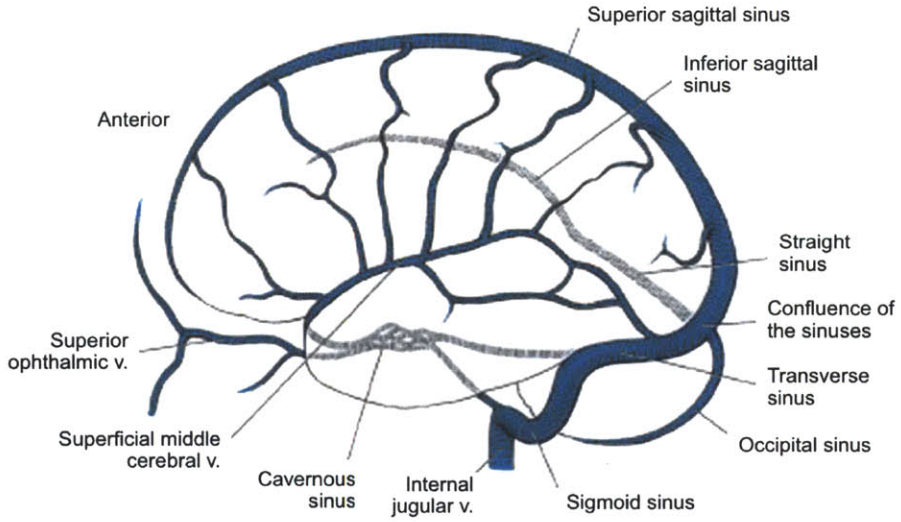

Figure 2-2: Cerebral blood circulation: veins [8].

Blood is drained from the brain via a venous system that can be separated into superficial and deep subsystems, Fig. 2-2. The superficial system contains venous sinuses that are located on the surface of the cerebrum, the most prominent of which is the superior sagittal sinus. At the confluence of sinuses, the superficial and deep drainage systems join. From this intersection, two transverse sinuses wrap laterally around the cerebrum in an S-shape, forming the sigmoid sinuses and continuing into the two jugular veins. These veins then drain blood into the superior vena cava, leading to the heart.

2.1.1 Cerebrospinal Fluid and ICP

While the vascular system supplies the brain with necessary nutrients and transports wastes, another important requirement for the brain is mechanical cushioning. As the

seat of all neurological functions, the brain and delicate neural tissue must be buffered from sudden impacts and compressive damage. This buffering job is accomplished by the cerebrospinal fluid which in turn exerts pressure, also known as ICP, in the cranial space.

Cerebrospinal Fluid

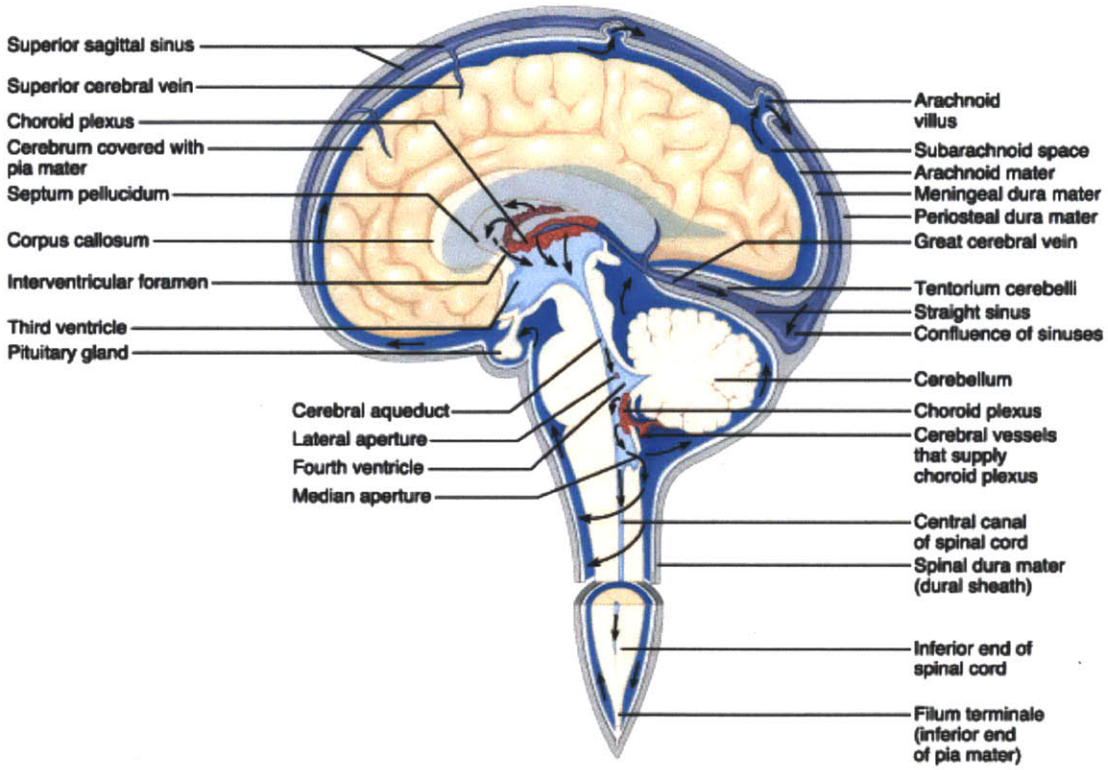

Figure 2-3: Diagram of a cerebral sulcus showing subarachnoid cavity, or space, and surrounding pia mater and arachnoid membrane [15].

The brain floats within the skull, cushioned and surrounded by CSF [16]. CSF occupies the subarachnoid space, Fig. 2-3, filling ventricles, sulci and the central canal of the spinal cord. In addition to serving as a mechanical buffer, CSF also acts as a chemical buffer, flowing throughout the brain and filtering metabolic waste through the blood-brain barrier. CSF is produced from the capillaries along ventricular walls at a slow rate of less than 0.1 mL/min. CSF is continuously reabsorbed into

the bloodstream via small protrusions in the arachnoid membrane, called arachnoid granulations, and is replenished about 3 to 4 times during the course of a day [17].

Intracranial Pressure

The pressure exerted by CSF in the cranial space is known as intracranial pressure (ICP). ICP is normally between 7-15 mHg, and can rise as high as 20-25 mmHg before intervention is necessary. Changes in ICP are due to changes in the fluid volume or total volume in the cranium. Typically, autoregulation maintains a constant cerebral perfusion pressure (CPP), which is the pressure gradient driving blood flow through the brain. CPP is the difference between mean arterial pressure (MAP) and ICP: CPP = MAP − ICP. However, abnormally low MAP or high ICP can cause a reduction of blood flow to the brain and a lack of oxygenation of cerebral tissue, inducing the body's natural response to increase blood volume to the brain by dilating the cerebral vasculature. This in turn increases ICP. Such a harmful positive feedback loop can exacerbate the stress on the brain.

Brain injury can cause dangerous elevation of ICP, often requiring interventions to relieve increasing pressure. Strokes resulting in hemorrhage and unilateral hematomas can cause a midline shift of the brain to one side. Another serious risk is the buildup of pressure gradients, resulting in brain herniation, where brain tissue is forcefully compressed, potentially leading to death. In addition to acute head trauma, abnormalities occurring on longer timescales can also raise ICP. Blockage of CSF drainage due to either disease or impaired reabsorption is a condition called hydrocephalus, and slowly increases volume and ICP. Brain tumors and lesions can also cause ICP to increase, and if left unchecked, can eventually shift the entire brain.

When ICP is elevated, the first priority is to reduce ICP. Interventions can be as simple as inducing hyperventilation or raising the patient's head. Hyperventilation decreases carbon dioxide levels, inducing constriction of blood vessels and reduction of cerebrovascular volume, thus relieving ICP somewhat. Raising the head can improve venous drainage, reducing fluid volume and pressure in the cranium. Serious swelling, however, may require chemical interventions such as administration of an-

tihypertensive agents, which work to decrease MAP. Mechanical interventions may also be necessary, such as: craniotomies, where holes are drilled in the skull to allow CSF extraction, and decompressive craniectomies, where entire sections of the skull are removed to allow the brain to swell. These are both last-resort procedures to relieve pressure from parts of the brain and to allow brain swelling without risk of tissue compression.

2.2 Simplified Model and Time Domain ICP Estimation Algorithm

The cerebral physiology reviewed above has been represented by simplified models such as the ones introduced in Chapter 1. In this section, we give an overview of the lumped, two-element model and corresponding TD ICP estimation algorithm presented in [14].

2.2.1 Simplified Model of Cerebrovascular System

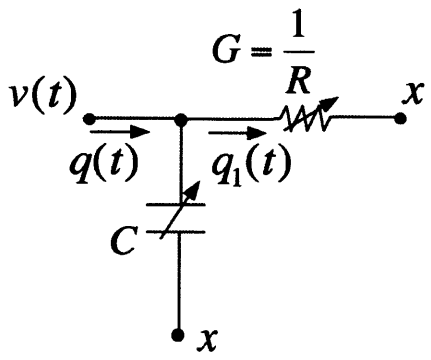

Figure 2-4: Simplified cerebrovascular model from [14].

Kashif et al. represent the cerebrovascular system in an electrical analog form, as a resistor-capacitor circuit, Fig. 2-4. The model takes blood flow through a cerebral artery, denoted by $q(t)$, and arterial blood pressure at that cerebral artery, denoted by $v(t)$, as the two inputs. Arterial and venous resistance of the cerebral vasculature

are represented by R (or conductance G), and compliance of the cerebral arteries and the surrounding brain tissue is represented by C. Downstream pressure at the level of cerebral veins, which are collapsed de to the Starling resistor behavior, is represented as ICP, or x. The Starling resistor effect is observed because ICP is typically higher than the venous pressure, causing cerebral veins to collapse and thus making the effective downstream pressure ICP rather than venous pressure [18]. R and C vary in time, capturing the automatic regulation of blood flow via blood vessels changing their muscle tone. During a beat period or even a multi-beat estimation window, the physiological parameters are assumed to be constant.

2.2.2 Overview of Time Domain ICP Estimation Algorithm

The TD ICP estimation algorithm presented in [14] operates on pulsatile input waveforms, and can produce one ICP estimate per cardiac cycle or per window of 5-60 cardiac cycles. The algorithm estimates ICP in a two-step fashion. First, the physiological parameter C is estimated. Then, the estimate of C is back-substituted into the simple model to estimate R and ICP. We briefly outline the algorithm steps below.

1. Input data waveforms of arterial blood pressure (ABP) and cerebral blood flow velocity (CBFV) are annotated for beat onsets. CBFV is assumed to be proportional to cerebral blood flow; proportionality suffices to enable the approach in [14].

2. C and R are estimated during each cardiac cycle. During the sharp transitions in $v(t)$, $q(t)$ flows primarily through the compliance branch. Thus the model simplifies to a capacitor-only branch, and we can estimate C easily. After obtaining C, we estimate blood flow $q_1(t)$ through the arterial resistance, and then estimate R based on two time-instants of arterial blood flow and pressure. Estimation of R and C are detailed in [2].

3. R is then back-substituted into an expression relating ICP and arterial pressure, and we obtain an ICP estimate for the given cardiac cycle.

2.2.3 Measurements

We briefly describe the two input waveforms used in TD ICP estimation. The estimation algorithm operates on pulsatile ABP and CBFV waveforms, $v(t)$ and $q(t)$, respectively. An example of each is shown in Fig. 2-5 over a few beat periods in order to describe intrabeat morphology, with beat onsets annotated in red circles.

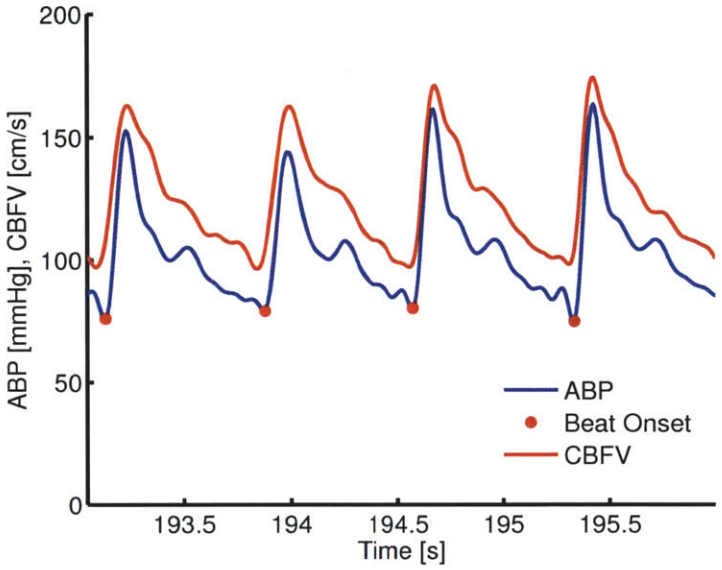

Figure 2-5: Example of pulsatile input data. ABP is shown in blue, CBFV shown in red, and beat onsets are marked with red circles.

Note that each waveform approximately follows a predictable pattern over a beat interval; we consider the ABP waveform for convenience in this discussion, but the pattern extends to the CBFV waveform. For each cardiac cycle, the heart fills with blood during the period called diastole, and contracts during systole, forcefully ejecting deoxygenated blood into the lungs and oxygenated blood into the aorta. The aorta subdivides into the arterial network, and ABP is measured at the radial artery. The beat onset annotations mark the beginning of systole, during which blood pressure rises rapidly from end diastolic pressure to systolic pressure at the peak of the waveform. After peak systolic pressure is reached, diastole begins and the heart fills with blood while pressure steadily decreases to end diastolic pressure. The cycle then begins anew.

The ABP and CBFV waveforms contain small fluctuations. These small fluctuations are analogous to reflections of a pulse along a transmission line. Due to the mechanical properties of blood vessels, we can regard the vasculature as a network of transmission lines, and thus expect small reflections of the peak pressure to propagate within a beat interval. While small fluctuations, especially the prominent reflection in ABP occurring approximately halfway during diastole, are regarded to be normal, very rapid fluctuations can sometimes be attributed to instrumentation noise during data acquisition. Such noise is actually very undesirable for algorithm performance, as this noise propagates through the steps of the algorithm, and can be amplified in the final ICP estimate.

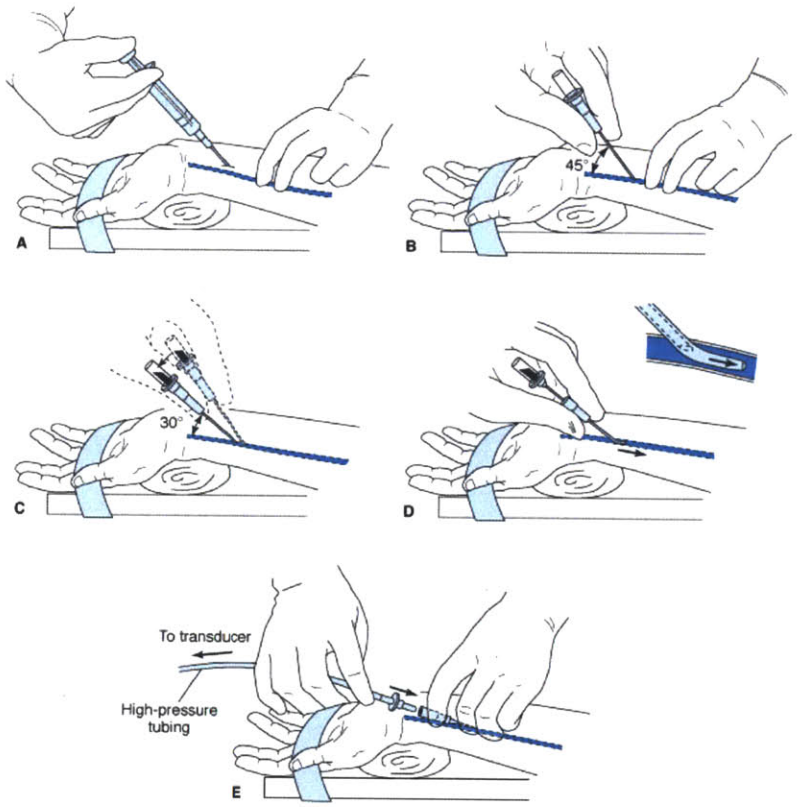

Figure 2-6: Radial artery cannulation [19].

The input waveforms of ABP and CBFV are currently acquired in a minimally- and noninvasive fashion, respectively. ABP is acquired at the wrist via cannulation of the radial artery. While somewhat invasive, radial artery cannulation is a routine

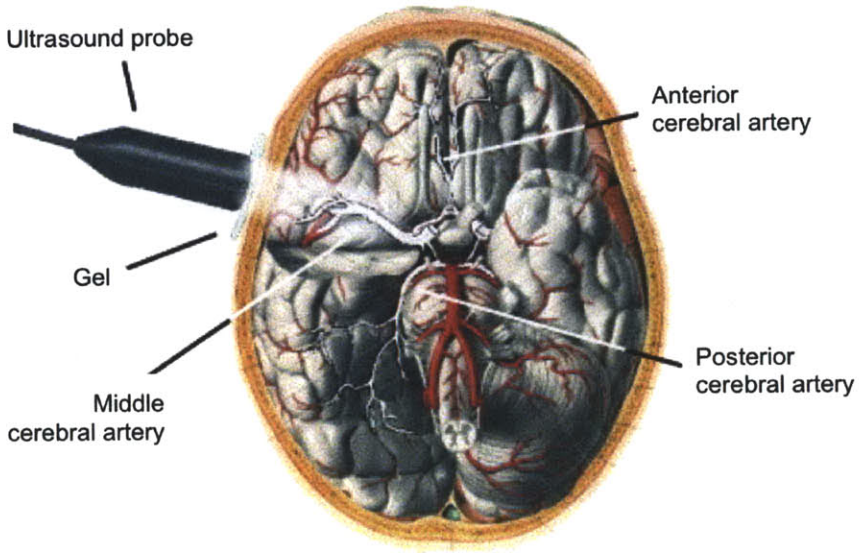

Figure 2-7: TCD insonation [20].

procedure performed on almost all patients admitted in the neuro-intensive care unit, and causes little discomfort or complication. A cartoon of radial artery cannulation is shown in Fig. 2-6. CBFV is measured at the MCA via transcranial Doppler (TCD) ultrasound, Fig. 2-7. While TCD is not frequently acquired for all patients, CBFV acquisition is completely noninvasive and pain free. For several neurological conditions, such as subarachnoid hemorrhage, TCD is actually part of standard care. It does, however, require some technical expertise for proper placement at the target, and thus can be a source of error. Because CBFV is measured at the MCA, it is a direct substitute for the desired model input waveform $q(t)$, blood flow into the cerebrovascular system. Although CBFV is blood flow velocity, and not the desired quantity cerebral blood flow, CBFV and $q(t)$ are approximately related via a simple scaling factor. The ICP estimate is not affected by this scale factor.

2.3 Summary and Preview

We have provided a quick review of the cerebrovascular physiology. We have also briefly reviewed the pathophysiology and consequences of elevated ICP. We then described the simplified model of the cerebrovascular system and the ICP estimation

approach proposed in [2]. In the following chapters, we explore alternatives for finding the model parameters via frequency domain representation.

Chapter 3

Frequency Domain Parameter Estimation

We present in this chapter a frequency domain (FD) parameter estimation algorithm. We discuss investigations pertinent to honing components of the algorithm, and conclude with an overview of precise parameter values used in the FD algorithm.

3.1 Development of the Frequency Domain Parameter Estimation Algorithm

The FD approach to estimating parameters transforms the simplified cerebrovascular system model into the frequency domain and examines the relationship between model parameters and measurements. Referring to the dynamic model in Fig. 2-4, the equivalent FD representation is given by

$$Q(\omega) = V(\omega)(G + j\omega C) - GX(\omega), \tag{3.1}$$

where $X(\omega)$, $V(\omega)$ and $Q(\omega)$ are the Fourier transforms of $x(t)$, $v(t)$, and $q(t)$, respectively. As in TD estimation, the FD ICP estimation algorithm operates on pulsatile ABP and CBFV waveforms. We assume that ICP is essentially constant over a cardiac beat cycle, and also over estimation windows of reasonably short duration; G

and C are similarly constant over that window. The assumption that physiological parameters, including ICP x, are constant over an estimation window allows us to consider $X(\omega)$ as zero for nonzero ω. This allows (3.1) for $\omega \neq 0$ to be simplified to

$$V(\omega)(G + j\omega C) = Q(\omega). \tag{3.2}$$

We show in the next subsection how (3.2) can be used to estimate parameters C and G. Our ICP estimate is then obtained in terms of input waveforms averaged over the estimation window:

$$x = \overline{v(t)} - \frac{\overline{q(t)} - C\overline{\frac{dv}{dt}}}{G}. \tag{3.3}$$

Now we turn our attention to estimating C and G.

Parameter Estimation

Since $X(\omega) = 0$ for all $\omega \neq 0$, rewriting (3.1) for different ω values yields the following system of equations:

$$\begin{bmatrix} j\omega_1 V(\omega_1) & V(\omega_1) \\ j\omega_2 V(\omega_2) & V(\omega_2) \\ \vdots & \vdots \\ j\omega_n V(\omega_n) & V(\omega_n) \end{bmatrix} \begin{bmatrix} C \\ G \end{bmatrix} = \begin{bmatrix} Q(\omega_1) \\ Q(\omega_2) \\ \vdots \\ Q(\omega_n) \end{bmatrix} \tag{3.4}$$

for $\omega_1, \omega_2, \ldots, \omega_n \neq 0$. For ease of reference, we denote the first matrix as F, the parameter vector as z and the vector on the right side as g; thus $Fz = g$ corresponds to (3.4) above. Recall that $V(\omega)$ and $Q(\omega)$ have both real and imaginary terms. Separating the real and imaginary parts of F and g and concatenating the two sets of equations as

$$\begin{bmatrix} \Re\{F\} \\ \Im\{F\} \end{bmatrix} z = \begin{bmatrix} \Re\{g\} \\ \Im\{g\} \end{bmatrix}, \tag{3.5}$$

we solve this system of equations via a least-squared error criterion. Solving for C and G in this way constrains C and G to real values while still taking into account both the real and imaginary components of the input data frequency spectra.

Ideally, only two ω values are needed from which C and G can be calculated accurately. The complexity of input waveforms, however, makes selection of only two frequencies difficult since valuable information is not limited to single frequencies. Instead, (3.1) is populated by selecting a range of frequencies. The frequency range selection process is detailed in Appendix A. Our final frequency range choice encompasses the first two heart rate frequency (HRF) peaks, ranging from $0.9 \times$ HRF to $2.1 \times$ HRF, and we consider each frequency individually. A visual example of HRF peaks is shown in Fig. 3-1.

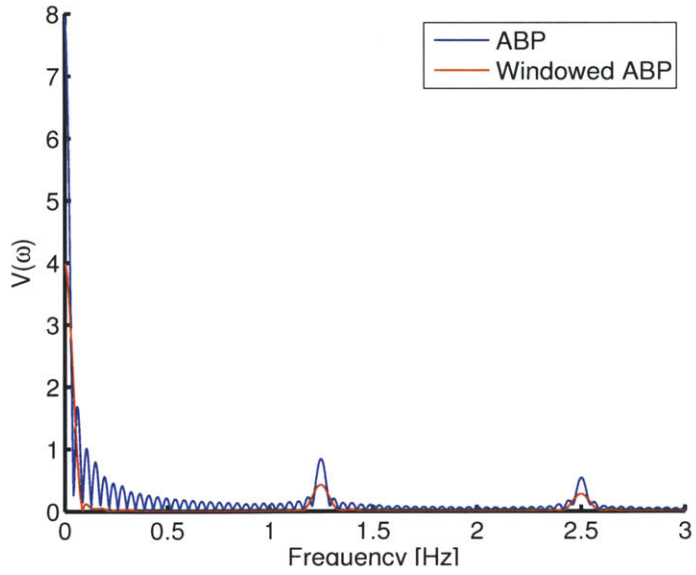

Figure 3-1: Input waveform frequency spectra showing HRF peaks at 1.25 Hz and its harmonics.

3.2 Preprocessing Steps

Input waveforms must be preprocessed prior to ICP estimation. Preprocessing serves several important purposes: to homogenize input data sampling frequency, to annotate beat onsets and label sections of poor signal quality, to generate offsets for

approximating cerebral ABP from radial ABP, and to account for frequency domain effects of windowing in the time domain. In this section we describe each of the preprocessing steps and report our findings from investigations regarding these steps.

3.2.1 Resampling and Beat Onset Detection

The first preprocessing step performed on all input data is resampling. As is common in hospitals due to proprietary quirks of medical devices, the input data we analyze are recorded at a wide variety of sampling frequencies, ranging from 20 to 70 Hz. We upsample all data to 125 Hz; as a result, our frequency spectrum calculated via the Fourier transform will range from -62.5 up to 62.5 Hz. Next, a beat-onset detection algorithm is applied in order to demarcate beat intervals [21]. Placement of beat onset location additionally gives access to intrabeat information, such as heart rate and mean values within a beat interval. Data is also reviewed visually in order to ensure that extensive breaks or disruptions in data are labeled appropriately, and that these sections are automatically excluded from ICP estimation.

3.2.2 Time-Offset Estimation

The simplified model relates CBFV $q(t)$ and ABP $v(t)$ to ICP estimate x as

$$q(t) = C\frac{dv(t)}{dt} + \frac{v(t) - x}{R}. \tag{3.6}$$

Method 1:

The $v(t)$ in (3.6) is arterial pressure at the MCA, but our pressure measurement is at the radial artery (RA). We time-shift the RA measurement to get a better approximation to the desired MCA pressure waveform. Equation (3.6) shows that at low frequencies the model acts like a purely resistive circuit. Thus, the low-frequency spectrum of the shifted RA waveform can be approximated as a scaled version of the CBFV waveform, when the appropriate time offset is used. We therefore seek to minimize the angle between the low-frequency portions of the two spectra, and

correspondingly find the offset that maximizes the quantity

$$\cos(\theta) = \frac{|V^\dagger Q|}{\sqrt{V^\dagger V}\sqrt{Q^\dagger Q}} \tag{3.7}$$

where Q and V are complex vectors comprising the low-frequency portions of the Fourier Transforms of $q(t)$ and the shifted RA pressure, respectively, and $\dagger$ denotes the Hermitian transpose (i.e., the complex conjugate transpose). Because this approach searches for alignment of low-frequency components, we consider the V and Q containing frequency spectra information up to the first HRF. Within each window, we cycle through candidate offsets to find the best alignment, i.e., the highest $cos(\theta)$ in (3.7). We report one offset per window, and report the median over the entire record. Offsets are suggested as integer multiples of the sampling period or inverse sampling frequency–an offset value of 1 corresponds to .008 sec, offset value of 2 corresponds to .016 sec, etc.

Method 2:

Inspired by the second idea in the TD approach, alignment of the maximum time derivative of ABP with the peak amplitude of CBFV, is equivalent to bringing CBFV maximally out of phase with the shifted RA pressure for high frequencies. Thus, we seek to maximize the sine of the high-frequency phase difference between the two input data spectra. Selecting high-frequency components, we compute

$$\sum_n \sin\left(\omega_n(\angle Q(\omega_n) - \angle V(\omega_n)\right) \tag{3.8}$$

and record for each window the offset that results in maximum value of (3.8). The median offset over the entire record is reported. For this approach, we consider high-frequency data from $8 \times$ HRF up to $12 \times$ HRF.

The two methods were tested, and results are discussed in Appendix B. However, both methods were found to be unsuitable for estimating ICP due to non-physiological parameter estimates and high variability in suggested offsets, respectively. Thus, we will generate ICP estimates using candidate offsets generated by the TD time-offset

algorithms described in [14], which yield physiological estimates of C and G, and produce offset suggestions with low variability.

3.3 Overview

We have developed the frequency domain-based estimation algorithm for model parameters including ICP, and reviewed the preprocessing steps. We now present an overview of the FD ICP estimation algorithm, and reveal parameter choices. All simulations were performed in Matlab©.

1. Input data waveforms of ABP and CBFV are upsampled to 125 Hz. Upsampled waveforms are annotated for beat onsets and labeled for physiological anomalies.

2. Input data waveforms are used to calculate a time-offset via the TD offset estimation method from [14]. The RA pressure waveform is shifted appropriately by the median of suggested offsets in order to approximate MCA pressure.

3. Estimation windows are demarcated in both input waveforms. Each window extends over 30 cardiac cycles, and the windows are non-overlapping. Frequency spectra for each window are obtained via the Fast Fourier Transform (FFT).

4. Parameters C and G are estimated using the least-squares method described in Section 3.1, over a frequency range of $0.9 \times$ HRF to $2.1 \times$ HRF. All frequency data is weighted equally.

5. C and G are substituted into the ICP expression in (3.3). One ICP estimate is reported for each estimation window. If the ICP estimates are less than 0 mmHg, we adjust the time-offset until we have a physiological ICP estimate.

3.4 Summary

In this chapter, we presented the FD parameter estimation approach. We investigated a process for choosing these algorithm parameters, and gave an overview of the

approach. In the next chapter, we present the results of FD estimation and compare with invasive ICP measurements.

Chapter 4

Results and Discusison

In this chapter we present the results of FD parameter estimation for 28 patient records. We show examples of typical FD estimates in the first section, and present aggregate statistics in the form of a Bland-Altman plot. In the second section, we discuss the results of FD estimation and characterize FD algorithm performance. Examples of each performance category are shown and discussed in detail. We also compare FD estimation algorithm results with ICP measurements obtained via intraventricular probe, and with ICP estimates calculated via the TD estimation algorithm. In the third section, we discuss certain records that fail to perform well. We offer our observations and a tentative metric for pre-identifying records that are intractable to our current algorithms for FD estimation.

4.1 Results and Discussion

Records were taken from severe trauma patients at Addenbrooke's Hospital in Cambridge UK. The data was collected as part of routine clinical care. Use of the de-identified data for research was approved by the Neurocritical Care Users' Committee at Addenbrooke's Hospital and by the Massachusetts Institute of Technology (MIT) Institutional Review Board. Each patient record contains waveforms of ABP, CBFV from both the left (CBFVL) and right (CBFVR) MCA, as well as an invasive ICP measurement acquired via intraventricular probe. The length of records ranged from

approximately 6 minutes to 4 hours, for a total of approxiamtely 21 hours of data. Patient age for this group ranged from 17 to 67 years, with a median age of 29 years. Waveforms were recorded at sampling frequencies ranging from 20 to 70 Hz. For estimation, we blinded ourselves to the invasive measurement, and estimated ICP via the steps outlined in Chapter 3 using ABP and CBFVL waveforms. The following results were calculated using the TD-based time-offset calculation technique. Records for which ICP estimate was non-physiological, i.e. less than 0 mmHg, for more than 20% of the record were discarded and not considered in our aggregate analysis.

In order to compare measured ICP with FD algorithm estimates, we first define two broad categories of estimate performance: "accepable" and "unacceptable." Here, we define clinically "acceptable" as estimates that are physiological, i.e. most of the estimate is greater than 0 mmHg, and falling within a 10 mmHg range of error. We choose the latter constraint due to the error margin inherent in current invasive measurement devices. For example, the Spiegelberg probe used for intraparenchymal ICP monitoring was found to be within ± 10 mmHg of values reported by intraventricular monitoring for 96% of clinical comparisons [22]. Within the "acceptable" category, we further define "strongly accurate" estimates that are able to replicate virtually all physiological details of the invasive measurements. On the other hand, "unacceptable" records display none of these traits, and are typically non-physiological, deviate significantly from underlying trends in invasively measured ICP, and display errors in excess of 10 mmHg.

Over 28 patient records, 7 were discarded because we were unable to obtain physiological ICP estimates for a significant portion of the record. Of the remaining 21, 8 records met the criteria for acceptable records, while 13 records were unacceptable. Unacceptable records typically fell into two subcategories: estimates that followed physiological trends in measured ICP but were offset by greater than 10 mmHg for the entire records, or estimates that were both offset by greater than 10 mmHg and that did not follow salient physiological trends. We present representative examples of both broad categories of estimates, and discuss each example in detail.

4.1.1 Acceptable Estimates

Acceptable estimates fell into two subcategories: estimates that tracked physiological trends closely and were within 10 mmHg of the measured ICP for the entire record, and estimates that were within 10 mmHg of the measured ICP but tracked physiological trends poorly.

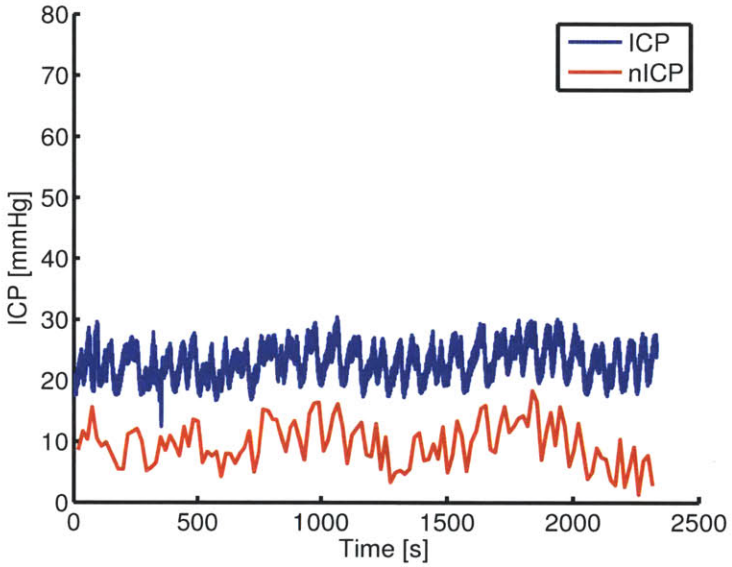

Figure 4-1: Acceptable record that tracks physiological trends very closely. Invasive ICP measurement is shown in blue, and FD algorithm estimate is shown in red.

Fig. 4-1 shows an example of an acceptable estimate that closely follows physiological trends. The measured ICP displays several interesting features: it is slightly elevated with a mean pressure of 23 mmHg, the waveform displays low-frequency oscillations on the order of 1 to 1.5 minutes in period, and there are also very low-frequency oscillations present with period on the order of a quarter of an hour. Note that the FD estimate tracks the latter two features very well; features such as a short plateau at approximately 250 seconds are replicated almost perfectly. The very low-frequency oscillations appear to be slightly exaggerated in the estimate as evidenced by the sharper dip around 1,250 seconds, and at 2250 seconds. Overall, the estimate performs very well, and one can imagine very accurate estimation with the application of an offset of approximately 10 mmHg in the vertical direction.

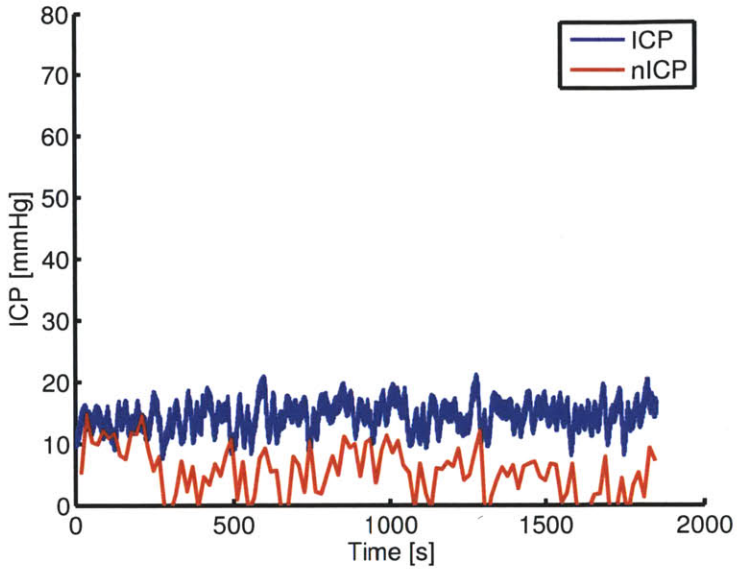

Figure 4-2: A second acceptable record.

A similar example with steady ICP and low-frequency oscillations is shown in Fig. 4-2. In this record, ICP levels are close to expected values of a healthy adult. The ICP is steadier than in Fig. 4-1 with fewer very low-frequency oscillations, but we observe similar oscillations with period on the order of a minute. These oscillations may be attributed to neurological phenomena, such as B-waves caused by oscillations in cerebrovascular volume [23]. This record also contains higher-frequency oscillations on the order of tens of seconds which are slower than respiratory frequencies. Note that the ICP estimate begins by slightly underestimating ICP, but adheres quite closely to ICP for the first approximately 200 seconds. After that time, the ICP drops sharply and consistently underestimates ICP, while still reflecting sharp fluctuations and oscillations in the measured ICP.

The measured ICP in the records in Figs. 4-1 and 4-2 have some intrinsic variability, i.e., the blue line indicating measured ICP is quite thick. This is as a result of respiration: during respiration, the volume and thus mechanical properties of the body change due to the emptying and filling of lungs with air. For the records shown in Figs. 4-1 and 4-2, the change in pressure due to respiration is approximately 3.5 mmHg.

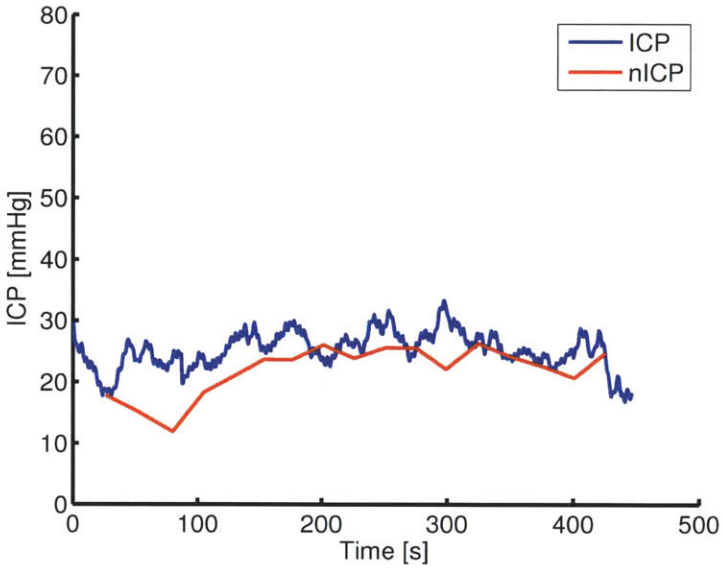

Figure 4-3: A third acceptable record that is higher in mean ICP amplitude, and rises and falls slowly over the duration of the record.

Figure 4-3 shows a record displaying elevated ICP that rises and falls approximately 10 mmHg over the 8 minute duration. This record displays an ICP of lower variability than the previous two examples, which is due to respiration causing a difference of only 1.5 mmHg in ICP. The estimate performs poorly at the second estimation window, at approximately 90 seconds, but recovers and tracks the ICP quite well for the remainder of the record.

Now we discuss acceptable estimates that do a poor job of tracking ICP trends. Fig. 4-4 shows an ICP estimate that is within the acceptable error range for the majority of the record. We can ignore the sharp spikes, which are due to noise artifacts in the input waveforms, and which we anticipate will be eliminated in future iterations of this algorithm. The notable feature of this record is that the ICP estimate does not follow any trends in ICP; in fact, it appears to diverge and follow exactly the opposite trend. For example, in the region from approximately 4,500 seconds to 6,000 seconds the ICP rises steadily from approximately 35 to 40 mmHg, while the estimate descends from 35 to 30 mmHg. Correspondingly, the peak at approximately 9,000 seconds and the drop at 4,000 seconds are not reflected in the estimate. In contrast, during those inflection points the estimate instead stays constant and rises,

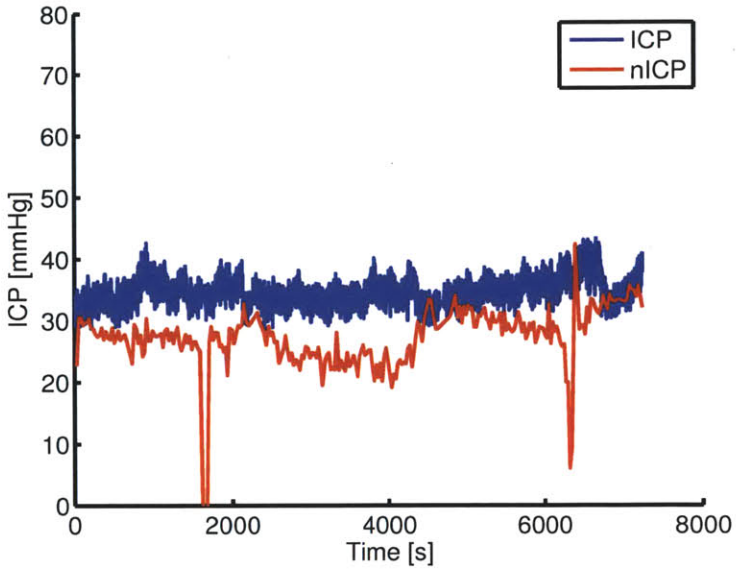

Figure 4-4: ICP estimate that is within the acceptable range of error, but tracks physiological trends poorly.

respectively.

The estimate in Fig. 4-5 does seem to follow the overall trend of rising steadily over the entire record. However, the undesirable feature of this record is the high variability. Although the estimates shown in Figs. 4-1 and 4-2 also possess considerable variability, the variability of the estimates does not exceed that of the measured ICP. In contrast, the variability in Fig. 4-5 is frequently twice or even three times the variability in the ICP measurement. Additionally, the estimate seems to be an exaggerated waveform; pronounced curvature is present from 750 seconds until the end of the record, while the ICP evolves in a linear fashion.

Other estimates seem to fall squarely between the two subcategories of acceptability, performing well in one section of the estimate and performing poorly in another. In Fig. 4-6, the ICP estimate does a very impressive job of tracking the measured ICP from approximately 7,500 seconds until the end of the record. In contrast, the start of the record is quite poor, and significantly underestimates the true ICP.

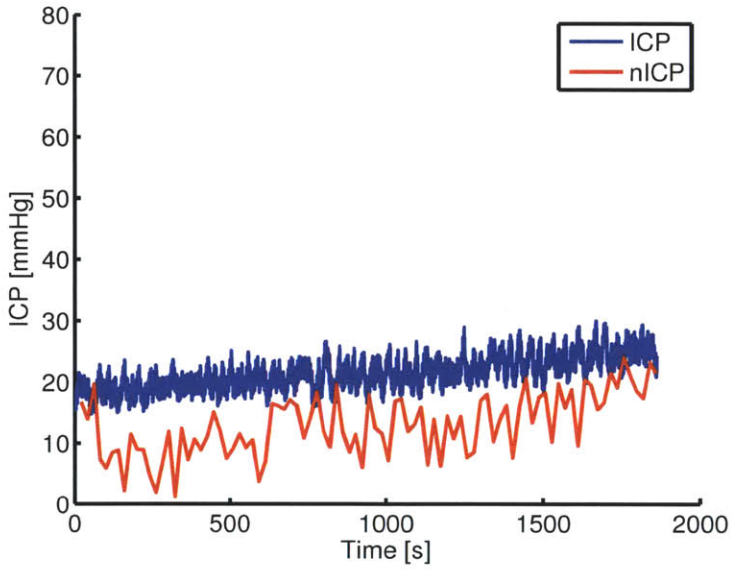

Figure 4-5: ICP estimate that is within the acceptable range of error, but displays high variability.

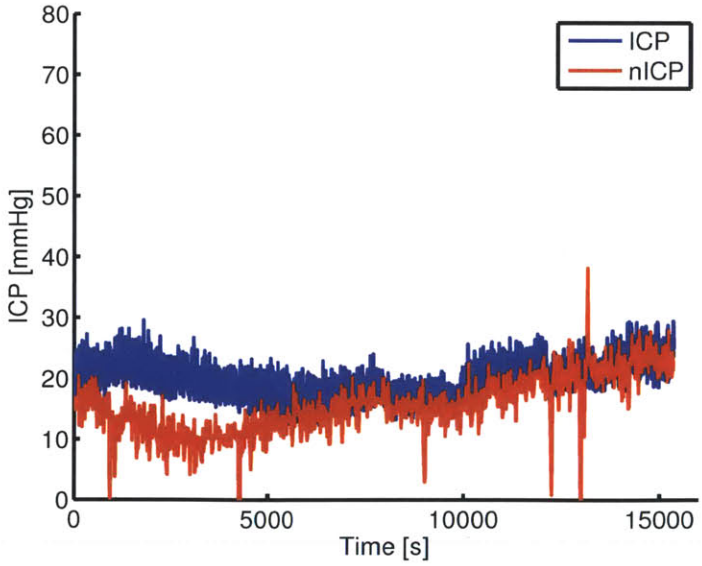

Figure 4-6: ICP estimate that is for the within the acceptable range of error and fairly accurate for the majority of the record, but does not track a significant portion of the ICP.

4.1.2 Unacceptable Estimates

We now discuss in detail several unacceptable estimates. As alluded to previously, the unacceptable estimates fall into similar subcategories: there are unacceptable estimates that are well outside the 10 mmHg error threshold, but track ICP trends faithfully, while there are also unacceptable estimates that are both far from the 10 mmHg error threshold and appear completely dissimilar to the measured ICP. We refer to these categories with records that have high bias and low dispersion, and records with high bias and high dispersion, respectively.

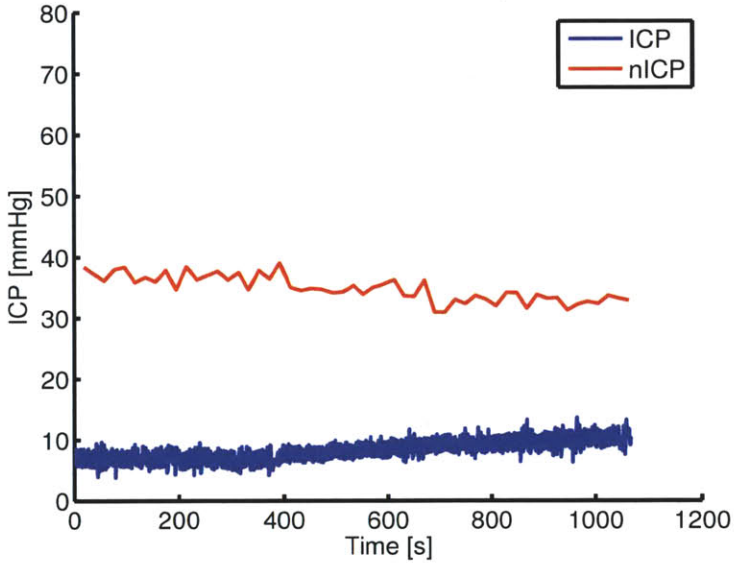

Figure 4-7: ICP estimate that is both outside the acceptable range of error and does not reflect any trends in ICP.

Figure 4-7 shows a quintessential unacceptable record, generated based on the candidate offset suggested by the TD offset algorithm. Errors are well in excess of 30 mmHg, and no physiological trend is retained in the estimate. Where the ICP goes up, the estimate goes down. Many of the unacceptable estimates appeared to similarly have "aloof" trends that had almost no similar features with the ICP measurement, and additionally changed little around an elevated mean value. We also obtained records that seemed to have a possible physiological basis, though we found no explanation. Fig. 4-8 shows a record that accentuates what are only hints

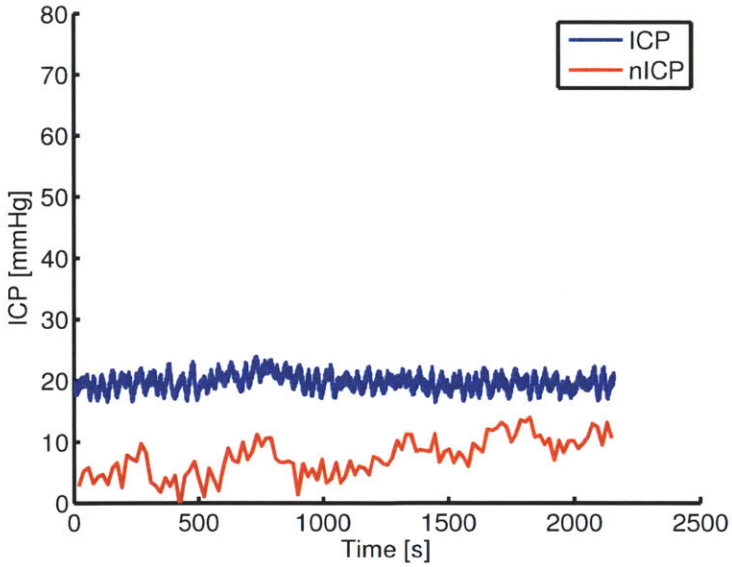

Figure 4-8: ICP estimate that exceeds the acceptable error threshold, and that accentuates features that are not particularly strong in the ICP measurement.

of curvature in the measured ICP.

There are also unacceptable records that are able to faithfully track ICP trends, but are simply too far offset vertically in order to be considered. Fig. 4-9 shows a record that does a remarkably good job of tracking the large parabolic swing in ICP, as well as the sharp notches at the beginning, midpoint, and end of the record. Large error in the beginning and especially the end segments, however, result in a very large error and disqualification of this record for the label of "acceptable." Similarly, the estimate in Fig. 4-10 does a very good job of tracking the many salient features of the ICP estimate. For example, the sharp rise beginning at 2,250 sec is well-represented in the ICP estimate, as is the dip at 2,750 sec. However, it is too far offset vertically from the ICP to be considered a successful estimate.

We have reviewed individual records and compared against invasive ICP measurements. We now review aggregate performance of all 21 records.

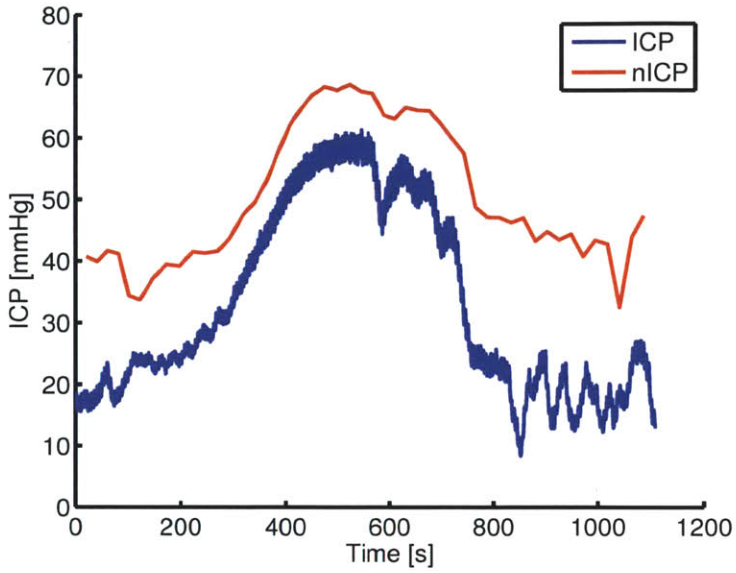

Figure 4-9: An ICP estimate that does a fine job of tracking physiological trends, but is too significantly offset from the ICP measurement to be considered acceptable.

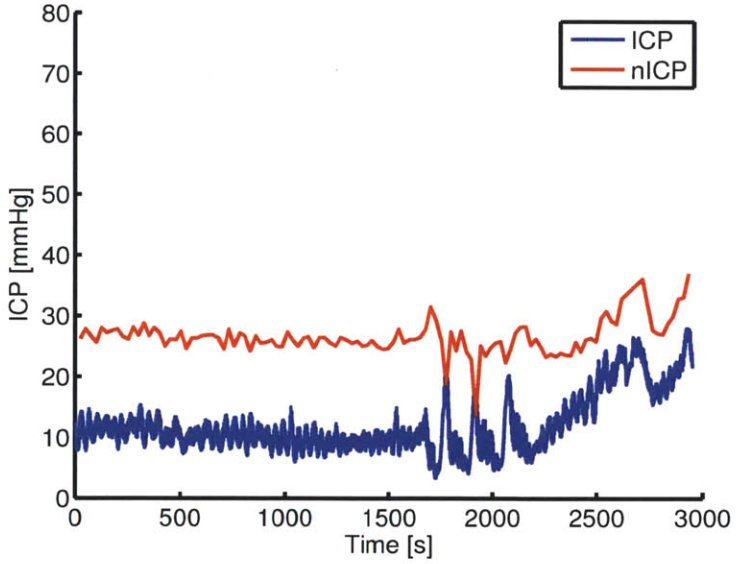

Figure 4-10: Another ICP estimate that also tracks physiological trends very well, but is significantly offset from the ICP measurement.

4.1.3 Aggregate Results

We evaluate ICP estimate performance on 21 patient records by comparing FD estimates with invasive ICP measurements. Since the FD algorithm produces one estimate per 30 beats, we compare the estimate with the mean of measured ICP taken over 30 cardiac cycles. To visualize the results, we present the data in the form of a Bland-Altman plot in Fig. 4-11, which is convenient for analyzing the agreement between two different methods [24]. Here, we compare the FD parameter estimation algorithm and invasive ICP measurement, and display mean ICP values on the horizontal axis and error on the vertical axis.

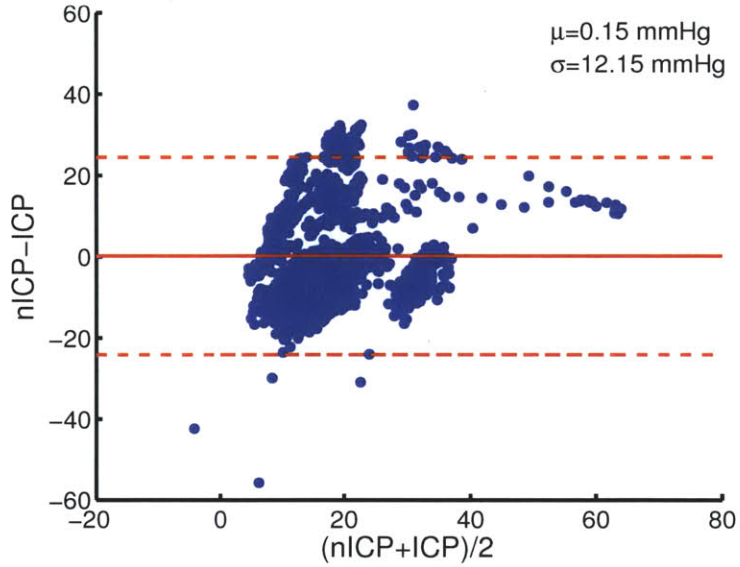

Figure 4-11: Bland-Altman plot for 21 records. Mean error is indicated by the solid red line, and twice the standard deviation above and below the mean are indicated by the dashed red lines. "nICP" is the abbreviation for noninvasive ICP estimate, and "ICP" refers to the invasive ICP measurement.

Each blue marker indicates one estimation window; for 21 records, we have approximately 2,700 estimation windows. ICP mean values are clustered from approximately 5 to 40 mmHg. The bias of 0.15 mmHg is of no consequence. The handful of large values of difference in estimated ICP as compared to invasive ICP measurement can be attributed to noise artifacts found in the input waveforms. We expect such noise artifacts to be eliminated in future iterations of the algorithm, which are better able

to check for breaks in data acquisition, etc.

While the mean error of the aggregate results is very low, the standard deviation is beyond the acceptable error for ICP monitoring. In addition, record-by-record comparison of estimates with invasive ICP waveforms shows that even in the best estimates, there is a bias error of at least 5 mmHg. From the wide variety of estimates reviewed, it is clear that are many factors that determine whether a given record of input data will produce accurate ICP estimates. We seek to obtain a higher fraction of estimates within the acceptable error range, and thus turn our focus to examining input data characteristics that may indicate *a priori* estimate bias or dispersion.

4.2 Observations

Our discussions focused on two estimate traits: bias and dispersion. These two traits are each affected by algorithm parameters and input data characteristics, and are sometimes unable to be decoupled. In this section, we present and review observations made regarding estimate traits. First, we review bias.

4.2.1 Estimate Bias

The estimate bias is the baseline, or mean value of the estimate error over the record. Of the various factors in the estimation algorithm, time-shift offset most directly affects estimate bias. Previously, we mentioned that time-shifts feasibly range from -20 to 20 multiples of the sampling period, and that positive offsets correspond to advancing the ABP waveform in time while negative offsets correspond to advancing the CBFV waveform. Within the feasible range, positive offsets also tend to correspond to vertical shifts of ICP, and likewise negative offsets shift the ICP to a lower bias. By adjusting the offset we can, for certain records, bring estimates into acceptable ranges. In some cases we can actually shift the bias of unacceptable records, such as the one in Fig. 4-10, into the realm of quite acceptable, Fig. 4-12.

Indeed, we have found through this sort of retroactive adjustment of the time-shift offset that we can occasionally obtain fairly accurate ICP estimates that far

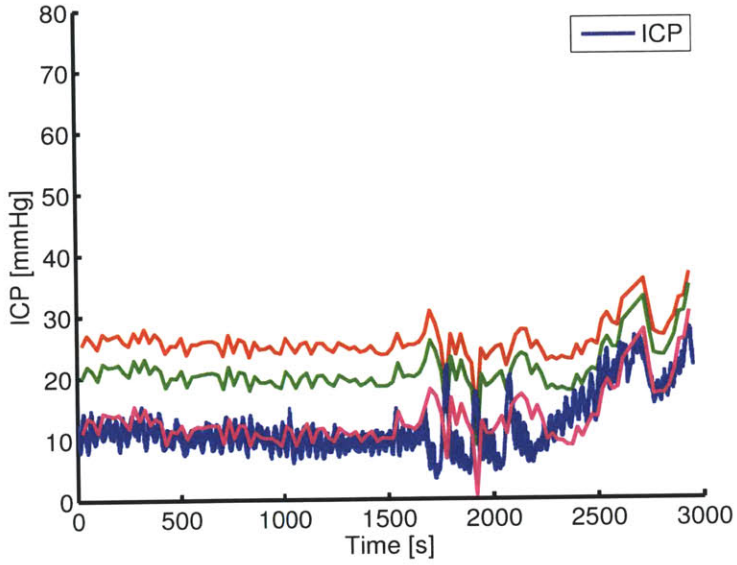

Figure 4-12: Results of adjusting time offset. The initial ICP estimate with a suggested time-offset of 0 is shown in red, ICP estimated with a shift of -2 is shown in green, and ICP estimated with a shift of -4 is shown in magenta.

outperform the estimates we initially calculated. However, while it is tempting to believe that offsets can in and of themselves change all estimate biases, there are two main obstacles to adopting such measures. The first is the physiological meaning of the offset. Our initial candidate offsets were generated in order to best approximate cerebral ABP from the available radial waveform. As such, wanton adjustment of the offset could result in estimates based on nonphysiological principles. The second caveat is that offset adjustment sometimes has absolutely no effect on certain patient records. The reason for this unknown, but it is an obvious impediment towards adopting arbitrary adjustments of offsets.

4.2.2 Dispersion

While obtaining an estimate with low bias is important, the dispersion of the estimate is just as critical. Clinicians are typically interested in only occasional measurements of ICP, and check ICP levels infrequently, on the order of hours. The boon of noninvasive ICP estimation, however, is that we produce estimates continuously, and thus can track the progression of intracranial hypertension. As such, producing estimates

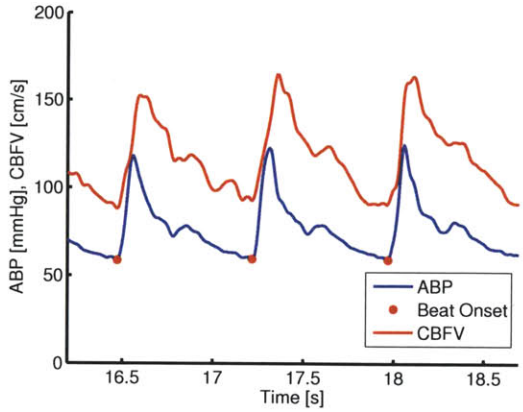

(a) Input data of an example unacceptable record. Note the notches in systolic peaks, and other noise, in the CBFV waveform.

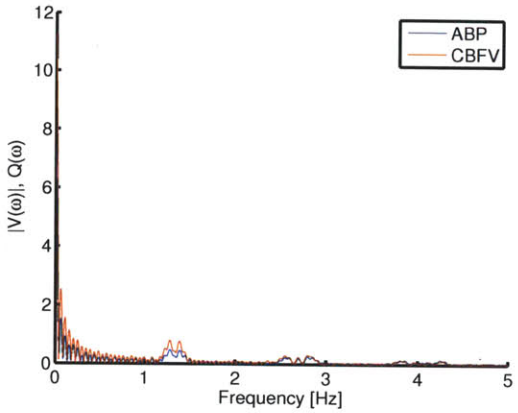

(b) Frequency spectrum displaying indistinct HRF peaks.

Figure 4-13: Input waveform features of a record that generated an unacceptable ICP estimate.

that accurately reflect trends in ICP is crucial. Correspondingly, preemptive determination that a record cannot be used to estimate a trend in ICP is important. In this section, we summarize our findings regarding the relationship between input data and estimate dispersion.

In order to determine the direct factors affecting dispersion, we examined the input data quality and the frequency spectra of the input waveforms. Recall that 7 of the initial 28 records produced nonphysiological estimates that could not be improved. Five of the 7 records yielded estimates with an extremely negative bias, and with high dispersion. Of the remaining 2 records, only one yielded an estimate that tracked the ICP measurement well. We found that the 5 records had both poor signal quality for CBFV, and frequency spectra with indistinct HRF peaks; an example of each feature is shown in Fig. 4-13.

To be precise, we define poor input data signal quality as input data that contains notches in systolic peaks such as that in 4-13a, or that contains high levels of noise. Interestingly, over half of the discarded records had ABP input waveforms of good quality. Thus, it appears that abnormal HRF peaks in the frequency spectra coupled with poor CBFV signal quality are sufficient indicators of ICP estimates with high

dispersion. However, as with any rule there are exceptions. We have found an example in which the converse case is true: the record shown in Fig. 4-3 is an example of an acceptable record with low dispersion, yet has a CBFV waveform with poor quality and contains very diffuse HRF peaks.

It also appears that having records with good CBFV signal quality and frequency spectra containing distinct HRF peaks does not necessarily guarantee a successful estimate. Thus, we discuss other factors that affect dispersion, one of which is the frequency range used to estimate C and G. For this thesis, we calculate ICP estimates using the frequency range including the first and second HRF peak, as well as the spectral data in between the peaks. Inclusion and exclusion of additional spectral data does affect the dispersion of the ICP estimate, but no direct correlations between spectral information and estimate characteristics have been established. The selection of frequency range also affects the effect of applied time-offsets. In order to better understand the decoupled effects of frequency range and time-offset, we suggest further investigations.

In this section, we investigated the factors contributing to the two main challenges in obtaining accurate ICP estimates. A trend of poor signal quality of input CBFV data and indistinct HRF peaks in the frequency spectra was found among 5 of the 7 discarded records. This trend may aid in preemptive identification of records that are unsuited to FD estimation, as currently implemented. However, given that we found several exceptions to this rule within the subset of 21 patient records that yielded physiological estimates, further investigation is required. In particular, we recommend that attention be focused on refining the frequency domain used for C and G estimation.

4.3 Summary of Results

In this chapter, we reviewed the results of FD parameter estimation. Aggregate results suggest that on average, overall performance of the FD estimation algorithm is adequate. However, examination of individual records and comparison to inva-

sive ICP measurements revealed that only 7 of 21 records yielded acceptable ICP estimates. While the results are not the encouraging outcome we initially desired, experimentation with algorithm components such as time-shift offset and frequency range selection has shown that it is possible to obtain very accurate ICP estimates. Furthermore, we were able to obtain a tentative rule for *a prior* determination of a record's potential to yield acceptable ICP estimates. In the following chapter, we recommend future work in order to improve the estimation approach.

Chapter 5

Conclusions and Future Work

This thesis presented an FD-based physiological parameter estimation algorithm. In the first chapter, we introduced current methods for ICP monitoring, and gave motivation for estimating ICP and other physiological parameters in the frequency domain. The second chapter outlined cerebrovascular physiology, and walked through the simplified cerebrovascular model and TD-based estimation algorithm in [2]. We then summarized development of the FD estimation algorithm in the third chapter, and presented representative examples, results, and a discussion of our results in the fourth chapter.

5.1 Summary

The work in this thesis began as a small academic project in order to provide an alternative method to TD ICP estimation presented in [14]. Based on the results of FD ICP estimation, that goal may not have been completely achieved yet. However, we have gained valuable information and intuition regarding ICP estimation in the frequency domain. The contributions of this thesis are the following:

- We have developed an FD parameter estimation technique for the model in [2].
- Considerable time and effort has been spent on analysis of frequency spectra of physiological signals. We have also gained intuition for FD analysis of physio-

logical signals.

- We have drawn conclusions regarding data characteristics that may help us better determine the ability to estimate ICP accurately. While these conclusions are tentative, future work should be focused on creating a definite metric for pre-estimation signal quality assessment.

- Although the FD estimation algorithm performance is not as successful as we initially desired, experiments with algorithm parameters have shown that it is possible to obtain extremely precise estimates by tweaking the algorithm pre-processing parameters. Thus, future work should also be focused on further explorations of algorithm parameters such as time shift estimation and frequency range selection.

5.2 Future Work

There are several facets of the FD ICP estimation algorithm that require further investigation, as well as several new channels of investigation that might improve ICP estimation.

Algorithm Parameter Investigation

As mentioned previously, we have obtained several tantalizingly accurate estimates from this FD estimation algorithm. However, since they were obtained "retroactively," that is, by adjusting the time offset to get a best fit to a known ICP measurement, they cannot be reported as algorithm results. Despite this, they offer a glimpse into the full potential of the FD estimation algorithm. The following points hold promise for improving the FD estimation algorithm.

- Crucial to both the TD and FD estimation algorithms, and estimation performance, is the time-shift estimation pre-processing algorithm. Recall that this step approximates the desired ABP at the MCA by a simple time shift of the available measurement of radial ABP. While this current strategy of

time-shifting the radial ABP waveform has yielded impressive results [14], this approximation does not account for various mechanical properties of blood vessels. The systemic arterial system is a complex branching network of blood vessels that bifurcates at each large artery into smaller arterioles and eventually capillaries, which then combine into venules and veins [25]. At each of these bifurcations, pressure waves reflect and combine with other traveling waves. These effects can be taken into consideration via numerical methods or finite-element models, for example. One such method, presented in [25], provides a method for estimating the shape of the ABP waveform at various large arteries. By adopting methods such as these, we can perhaps obtain a more accurate approximation of MCA ABP, and hope to improve ICP estimation.

- The vital component to the FD parameter estimation algorithm is the selection of the frequency range over which C and G are estimated. Our empirical selection of frequency range is based on the performance of a small subset of patient records. By examining a larger volume of patient records and doing an exhaustive analysis of the frequency spectra of all records, we can potentially obtain a more accurate frequency range for estimation of C and G. Furthermore, a more comprehensive understanding of frequency spectra can lend to a better pre-selection decision process that determines *a priori* whether or not a record is tractable for noninvasive estimation.

Bilateral Estimates

For this thesis, all results and algorithm tests were performed using radial ABP data, as well as CBFV data from the left MCA. In our possession is also the CBFV data from the right MCA. We suspect that estimation using both CBFV datasets could improve FD estimation performance, similar to the results of bilateral estimation shown in [26] and [14].

Finapres Data

The available ABP data we use is obtained via *minimally*, and not purely noninvasive techniques. In our possession is also ABP data obtained via a completely noninvasive Finapres© ABP finger cuff. Investigations with this noninvasive data could be fruitful for better understanding input data behavior, and could also lead to a better understanding of blood pressure waveform propagation through limbs and peripheral vasculature.

In sum, there remains significant future work to be done that may ultimately achieve the initial goal set forth by this thesis. This is but one small stretch on the road towards noninvasive ICP estimation, and it will be a rewarding path indeed.

Appendix A

Parameter Estimation

A.1 Closed Form Solutions of Parameter Estimation

We can find closed-form solutions for C and G by multiplying (3.1) by the Hermitian transpose of F, and separating the real and imaginary parts. Let us first consider the case of one specific ω. Thus, our complete expression for $F^\dagger Fz = F^\dagger g$ for ω is

$$\begin{bmatrix} j\omega V^*(\omega) \\ V^*(\omega) \end{bmatrix} \begin{bmatrix} j\omega V(\omega) & V(\omega) \end{bmatrix} \begin{bmatrix} C \\ G \end{bmatrix} = \begin{bmatrix} j\omega V^*(\omega) \\ V^*(\omega) \end{bmatrix} \begin{bmatrix} Q(\omega) \end{bmatrix} \tag{A.1}$$

where asterisks denote complex conjugates.

We separate (A.1) into its real and imaginary components, yielding (A.2) and (A.3), respectively:

$$\begin{bmatrix} \omega^2|V(\omega)|^2 & 0 \\ 0 & |V(\omega)|^2 \end{bmatrix} \begin{bmatrix} C \\ G \end{bmatrix} = \begin{bmatrix} \omega\left(V_R(\omega)Q_I(\omega) - V_I(\omega)Q_R(\omega)\right) \\ V_R(\omega)Q_R(\omega) + V_I(\omega)Q_I(\omega) \end{bmatrix} \tag{A.2}$$

$$\begin{bmatrix} 0 & -\omega^2|V(\omega)|^2 \\ \omega|V(\omega)|^2 & 0 \end{bmatrix} \begin{bmatrix} C \\ G \end{bmatrix} = \begin{bmatrix} -\omega\left(V_R(\omega)Q_R(\omega) + V_I(\omega)Q_I(\omega)\right) \\ V_R(\omega)Q_I(\omega) - V_I(\omega)Q_R(\omega) \end{bmatrix} \tag{A.3}$$

Equation (A.2) rearranges into the following closed-form solutions for C and G, which are referred to as the "real" solutions:

$$C = \frac{V_R(\omega)Q_I(\omega) - V_I(\omega)Q_R(\omega)}{\omega|V(\omega)|^2} \tag{A.4}$$

$$G = \frac{V_R(\omega)Q_R(\omega) + V_I(\omega)Q_I(\omega)}{|V(\omega)|^2} \tag{A.5}$$

Equations (A.4) and (A.5) thus yield C and G calculated from one value of ω. However, $V(\omega)$ and $Q(\omega)$ are nonzero for a wide range of ω, therefore we must consider (A.1) over a range of ω in order to obtain solutions of C and G. Taking into account all ω, we have the following real solutions:

$$C = \frac{\sum_n \omega_n[V_R(\omega_n)Q_I(\omega_n) - V_I(\omega_n)Q_R(\omega_n)]}{\omega_n^2|V(\omega_n)|^2} \tag{A.6}$$

$$G = \frac{\sum_n[V_R(\omega_n)Q_R(\omega_n) + V_I(\omega_n)Q_I(\omega_n)]}{\sum_n|V(\omega_n)|^2}, \tag{A.7}$$

and the following "imaginary" solutions derived from the complete form of (A.3):

$$C = \frac{\sum_n[V_R(\omega_n)Q_I(\omega_n) - V_I(\omega_n)Q_R(\omega_n)]}{\omega_n|V(\omega_n)|^2} \tag{A.8}$$

$$G = \frac{\sum_n \omega_n[V_R(\omega_n)Q_R(\omega_n) + V_I(\omega_n)Q_I(\omega_n)]}{\sum_n \omega_n|V(\omega_n)|^2}. \tag{A.9}$$

Note that evaluating (A.6) through (A.9) at any one value of ω results in (A.4) and (A.5), as expected. Note also that solving for C and G via this method yields the same results as solving for the parameters via least-squares error applied to (3.5).

A.2 Frequency Range Selection

Of central importance to solving for parameters C and G via least-squares error minimization is selection of the frequency range. Indeed, we require only two frequencies

in order to solve for two unknowns, but also wish to maximize the utility of available data in order to glean as much information as possible. Thus we consider the following:

- Computational feasibility: We envision an algorithm that is able to produce real-time estimates in a clinical setting. Although medical devices, and consumer electronic devices in general, are computationally more powerful than ever before, it is still beneficial to design algorithms that are not computationally taxing. For least-squares error minimization, we can choose from thousands of frequencies, but limit our frequency range to approximately 50 to 200 frequencies in order to drive down computational cost.

- Physiological considerations: It is known that physiological systems are limited to certain frequency ranges, e.g. heart rate typically falls between 60 and 120 bpm (approximately 1 to 2 Hz) for a healthy adult. Conversely, any signal above 20Hz is most likely noise, and not a physiological signal. As such, we can intelligently select a feasible frequency range, and limit our range accordingly. In addition, reviewing the frequency spectrum of the input waveforms has revealed information regarding power density of the signal. We observe that much of the signal's power is contained in heart rate harmonic frequencies (HRF). Thus, we select frequencies near or around these harmonic frequencies in order to ensure that we are using physiological data, and not simply noise.

- Applicability to large patient populations: While we can conjecture general ranges for physiological traits for all human patients, traits can vary significantly from patient to patient. We desire a frequency range that can adapt to specific patients, while still considering similar physiological characteristics across the entire population. Thus, we select relative, and not static or absolute frequency ranges. Frequency ranges used are multiples of the HRF, e.g. from $0.5 \times$ HRF to $2.5 \times$ HRF rather than fixed ranges, e.g. from 1 to 5 Hz.

Frequency ranges were tested in two ways. First, parameters C and G produced by the frequency ranges were compared to compliance and resistance estimates found

via the TD algorithm. Second, invasive ICP measurements were compared with FD ICP estimates calculated using test frequency ranges. After testing frequency ranges on several records, it was found that the optimal frequency range is 0.9 × HRF to 2.1 × HRF.

Frequency Data Weighting

Having defined the bounds of the frequency range, we evaluate point inclusion within that range. Since most of the frequency spectrum energy is found in the HRFs, it is difficult to tell whether there exists valuable frequency spectrum information in the regions between HRFs. We tested variations of the FD algorithm that included spectrum information from one HRF peak to the next, solely HRF peak information while excluding information between the peaks, or solely information between the peaks while excluding HRF peak information. In addition to region selection within the frequency range, we also explored use of peak "intensity" rather than use of all points within an HRF peak. Intensity is defined as the area under the HRF peak and approximated by

$$\Delta\omega_{\text{peak}} \sum_{i=\text{PBI}}^{\text{PEI}} V(\omega_i), \tag{A.10}$$

where "PBI" is the abbreviation for "peak beginning index" and "PEI" is the abbreviation for "peak end index." Through these investigations, we found that utilizing peak intensity led to higher variability within estimates. It was also found that use of exclusively data between HRF peaks also produced estimates with increased variability. Inclusion of both peaks and data between the peaks led to estimates which tended to be larger in magnitude, but with lower variability. Based on these investigations, we choose to use the frequency range encompassing the first two HRF peaks, 0.9 × HRF to 2.1 × HRF, and to consider each frequency individually, rather than using the intensity of HRF peaks.

Appendix B

Explorations of Preprocessing Steps

B.1 Candidate Offset Performance

In order to gauge the performance of candidate offsets suggested by the methods in Chapter 3, we perform two checks. First, we consider the variability of suggested offsets. Although small physiological variations can cause offset to change from beat to beat, we cannot expect the time-offset between radial and cranial ABP to fluctuate wildly, e.g. from 4 sampling periods to 20, corresponding to a difference in time-shift from 0.032 sec to 0.16 sec within the span of several cardiac cycles. Thus, low variability of suggested offsets is confirmation of a feasible candidate offset. We tested offsets ranging from -20 to 20, which are appropriate physiological lower and upper bounds, respectively, of time shifting. In order to maintain acceptable signal quality in the frequency domain, we tested offsets on input waveform segments of length 30 cardiac cycles. It was found that Method 1 generally produced offsets of low variability, while offsets produced by Method 2 were overwhelmingly variable. Fig. B-1 shows typical results of FD offset estimation: Method 1 suggested offsets are low in variability, while Method 2 offsets swing wildly from one window to the next. We also show an example of Method 2 with low variability in Fig. B-2.

In addition, we found that Method 1 produced nearly the same results no matter

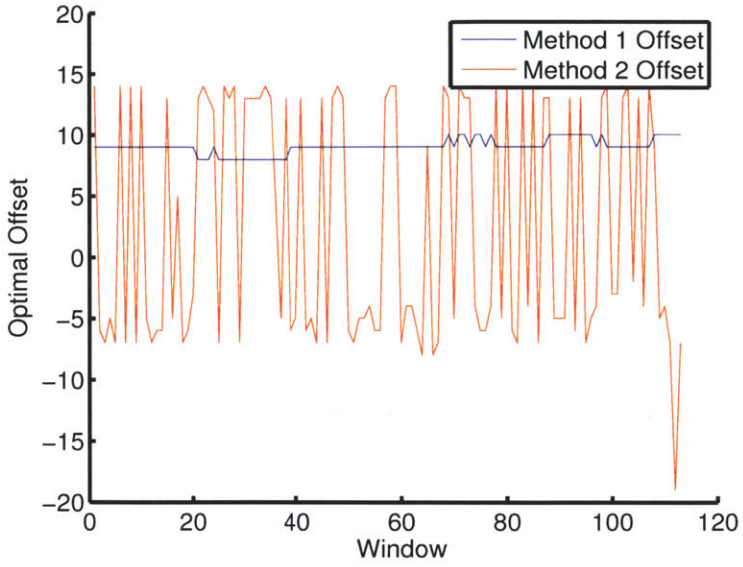

Figure B-1: Typical results of FD offset estimation. Method 1 suggested offsets in blue vary little from window to window, while Method 2 suggested offsets fluctuate significantly, often switching from -6 to 15, for example.

which precise low frequency range we selected; indeed, the suggested offsets were almost identical even if we chose to use the entire frequency spectrum up to 62.5 Hz. On the other hand, the frequency range used for Method 2 was found by testing various high frequency ranges on a few sample records until we found low variability. Thus, Method 2 is much less robust in FD estimation.

We also tested the practicality of candidate offsets by comparing shifted input waveforms. With Method 1, we expect to see low frequency components aligned; typical indications of low frequency alignment include alignment of systolic peaks, but alignment of cardiac cycle bases was also a good indication. For Method 2, we expect to see alignment of the CBFV systolic peak with the maximum upward rise of the ABP waveform. An example of successful alignment in both Methods 1 and 2 is shown in Fig. B-3.

The two methods performed differently in our two tests. Low variability in Method 2 was seen in only 6 of 28 total patient records analyzed, while low variability was seen in virtually all patient records for Method 1. This behavior may be a reflection of the high frequency range used for Method 2, since we selected the frequency range empir-

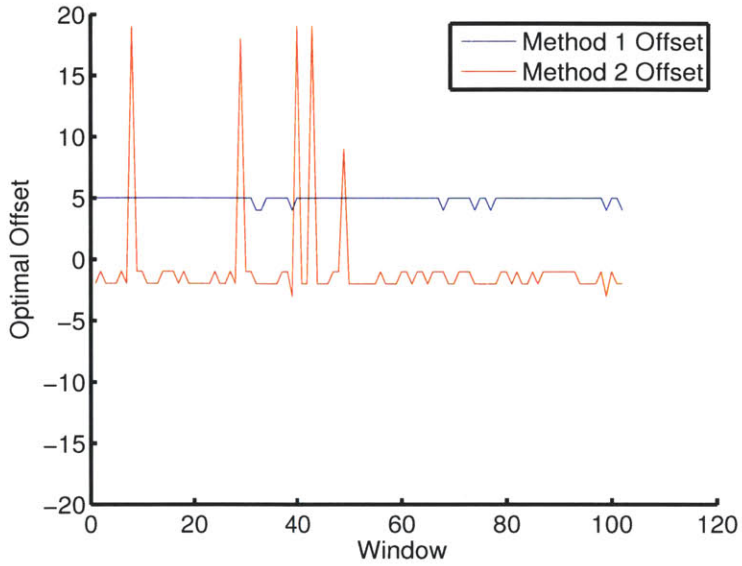

Figure B-2: Example of record with low variability in both Method 1 and Method 2 suggested offsets.

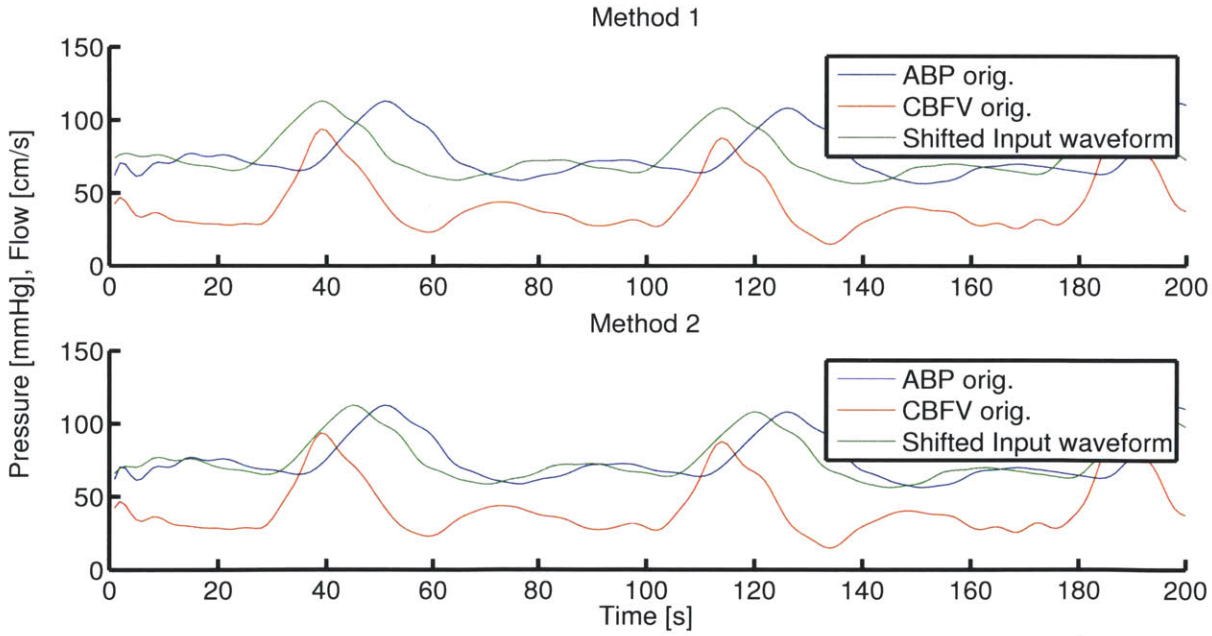

Figure B-3: Example of good alignment after shifting waveforms with median offsets from both Methods 1 and 2. Upsampled, unshifted input data waveforms of ABP and CBFV are shown in blue and red, respectively, while shifted waveforms of either are shown in green. Note that a positive offset corresponds to advancing ABP in time, or shifting the waveform left, while a negative offset corresponds to advancing the CBFV waveform in time.

ically based on the behavior of a few test records. Nevertheless, Method 1 appears to be a more robust method for calculating time offsets than Method 2. Furthermore, alignment of the input waveforms with the candidate offset from Method 2 yielded over twice as many poor results as did alignment with the Method 1 candidate offset.

Based on these tests, we generated several results using candidate offsets from Method 1, but do not use offsets suggested by Method 2. However, we found that these time-shifts resulted in primarily negative estimates of C. C is a physiological parameter, the compliance of the cerebrovasculature, and cannot be negative. Thus, although Method 1 yields reasonable candidate offsets, we cannot trust ICP estimates based on non-physiological parameters.

B.2 Windowing

The final preprocessing step concerns the transition from the time to frequency domain. It is a well known property of Fourier transforms that windowing of time domain signals, i.e. taking a segment of data for a region of interest in time and assuming all other time values to be zero, results in "smearing" of the frequency spectrum [27]. This is due to the fact that a sharply-defined window in time has Fourier transform that is a sinc function in frequency, extending infinitely in both $+\infty$ and $-\infty$ directions.

By the convolution property of Fourier transforms, one expects the frequency spectrum of any signal windowed in time to be a smoothed version of the un-windowed signal. Various window functions have been developed in order to compensate for this frequency-smearing effect. Common windows include the Hanning, Hamming, and Bartlett windows, each of which mitigates the effect of the infinitely-extending sinc function in exchange for reduced resolution and other spectrum trade-offs.

In the FD ICP estimation algorithm, we calculate one ICP estimate over a window of finite time span. Thus, we expect to see the effects of windowing in the frequency spectrum of the input waveforms, and in the frequency spectrum of the ICP estimate. We observed that the frequency spectra of many input waveform records contained a

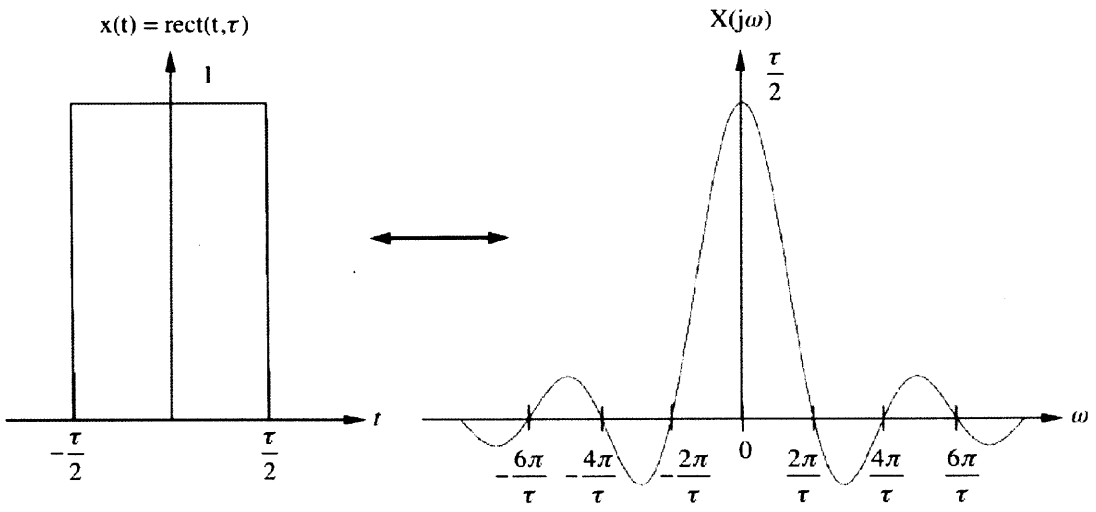

Figure B-4: Fourier transform relationship between a box function on the left and its sinc function transform pair.

fair amount of signal in the regions between the heart rate frequency peaks, especially in the region between 0 Hz and the first peak. While it is expected that these inter-peak regions can contain useful and valuable data, we suspected that the smearing effect of windowing might obscure the actual contribution of these regions. To test this, we applied several well-known time windows in order to mitigate potential windowing effects and compared the frequency spectra of input waveforms as well as ICP estimates before and after widowing. We tested Hamming and Hanning windows of variable length for each estimation window.

Fig. B-5 shows an example of input waveform frequency spectra prior to and after windowing. It is clear that application of a Hanning window, in this case, eliminates much of the noise between HRF peaks.

By simply observing the spectra, it is unclear whether or not this noise elimination is desirable. As mentioned previously, valuable data could be contained in the inter-peak regions, in which case we have performed excessive noise elimination. However, examination of ICP estimates obtained from windowed signal confirmed that application of windowing functions was too aggressive of a noise elimination technique. ICP estimates based on windowed signals contained much higher variability than those based on simple segments of data. In the best case, the window function parameters

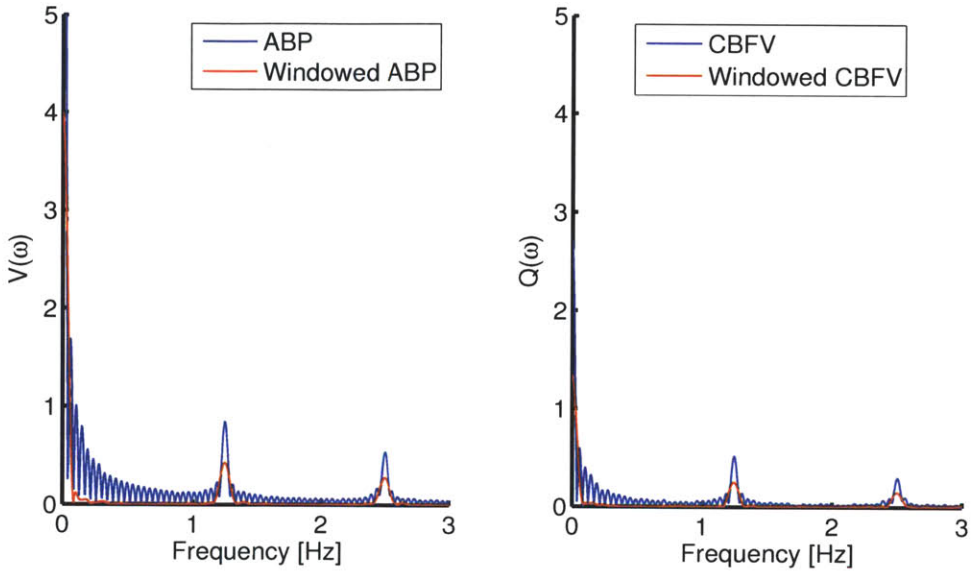

Figure B-5: Input waveforms before and after application of a Hanning window of same length as the estimation window.

could be adjusted such that the estimate variability decreased, but never exceeded the performance of un-windowed input waveforms. From these results, we determined that application of window functions is unnecessary.

Bibliography

[1] American Academy of Pediatrics and American College of Emergency Physicians. *The Pediatric Emergency Medicine Resource*, page 258. Jones and Bartlett Publishers, Inc., Burlington, MA 01803, 4th edition, 2005.

[2] Kashif FM. *Modeling and estimation for non-invasive monitoring of intracranial pressure and cerebrovascular autoregulation.* PhD thesis, Massachusetts Institute of Technology, 2011.

[3] Feldman Z and Narayan RK. *Head Injury*, pages 247–274. Williams and Wilkins, 1993.

[4] Raabe A, Stöckel R, Hohrein D, and Schöche J. An avoidable methodological failure in intracranial pressure monitoring. *Acta Neurochirurgica Supplement*, 71:59–61, 1998.

[5] Banister K, Chambers IR, Siddique MS, Fernandes HM, and Mendelow AD. Intracranial pressure and clinical status: assessment of two intracranial pressure transducers. *Physiological Measurement*, 21:473–479, 2000.

[6] Miller JD. Inaccurate pressure readings for subarachnoid bolts. *Neurosurgery*, 19(2):253–255, 1986.

[7] Kerr M and Crago EA. *Medical-Surgical Nursing: Assessment and Management of Clinical Problems.*, pages 1491–1524. CV Mosby Inc, St Louis, Mo, 2004.

[8] Kandel ER, Schwartz JH, and Jessell TM. *Principles of Neural Science.* McGraw-Hill, New York, 4th edition, 2000.

[9] Brain Trauma Foundation. *Guidelines for the Management of Severe Traumatic Brain Injury.* Mary Ann Liebert, Inc. publishers, 3rd edition, 2007.

[10] Ragauskas A, Daubaris G, Dziugys A, Azelis V, and Gedrimas V. Innovative non-invasive method for absolute intracranial pressure measurement without calibration. *Acta Neurochirurgica Supplement*, 95(357-361), 2005.

[11] Hu X, Subudhi AW, Xu P, Asgari S, Roach RC, and Bergsneider M. Inferring cerebrovascular changes from latencies of systemic and intracranial pulses: a model-based latency subtraction algorithm. *Journal of Cereb Blood Flow Metabolishm*, 29:688–697, 2009.

[12] Sorek S, Bear J, and Karni Z. Resistance and compliance of a compartmental model of the cerebrovascular system. *Annals of Biomedical Engineering*, 17:1–12, 1989.

[13] Ursino M and Lodi CA. Interaction among autoregulation, co2 reactivity, and intracranial pressure: a mathematical model. *American Journal of Physiology - Heart and Circulatory Physiology*, 174:1715–1728, 1998.

[14] Kashif FM, Verghese GC, Novak V, Czosnyka M, and Heldt T. Model-based noninvasive estimation of intracranial pressure from cerebral blood flow velocity and arterial pressue. *Science Translational Medicine*, 4(129), 2012.

[15] Marieb EN. *Essentials of Human Anatomy and Physiology.* Benjamin Cummings, 8th edition, 2006.

[16] Diagrammatic representation of a section across the top of the skull, showing the membranes of the brain, etc. `Wikipedia.org`.

[17] Cutler RW, Page L, Galicich J, and Watters GV. Formation and absorption of cerebrospinal fluid in man. *Brain*, 91:707–720, 1968.

[18] Chopp M and Portnoy HD. Starling resistor as a model of the cerebrovascular bed. In Ishii I and Nagai H, editors, *M. eds. Intracranial Pressure V*, pages 174–179. Springer-Verlag, Berlin, Heidelberg, 1989.

[19] Morgan G, Mikhail M, and Murray M. *Clinical Anesthesiology.* McGraw-Hill Medical, 4th edition, 2005.

[20] Deppe M, Ringelstein EB, and Knecht S. The investigation of functional brain lateralization by transcranial doppler sonography. *NeuroImage*, 21(3):1124 – 1146, 2004.

[21] Zong W, Heldt T, Moody GB, and Mark RG. An open-source algorithm to detect onset of arterial blood pressure pulses. *Computational Cardiology*, 30:259–262, 2003.

[22] Chambers IR, Siddiqui MS, Banister K, and Mendelow AD. Clinical comparison of the spiegelberg parenchymal transducer and ventricular fluid pressure. *Journal of Neurology, Neurosurgery & Psychiatry*, 71:383–385, 2001.

[23] Auer LM and Sayama I. Intracranial pressure oscillations (b-waves) caused by oscillations in cerebrovascular volume. *Acta Neurochirurgica*, 68:93–100, 1983.

[24] Bland JM Altman DDG. Measurement in medicine: the analysis of method camprison studies. *The Statistician*, 32:307–317, 1983.

[25] Sherwin SJ, Franke V, and Peirò J. One-dimensional modelling of a vascular network in space-time variables. *Journal of Engineering Mathematics*, 47:217–250, 2003.

[26] Hwang IT. Characterization of a non-invasive intracranial pressure estimation algorithm. Master's thesis, Massachusetts Institute of Technology, May 25 2011.

[27] Oppenheim AV and Schafer RW. *Discrete-Time Signal Processing.* Pearson Higher Education, Inc., Upper Saddle River, NJ 07458, 3rd edition, 2010.